Check for updates

JAMES | Journal of Advances in Modeling Earth Systems

RESEARCH ARTICLE
10.1029/2022MS003579

Climate, Variability, and Climate Sensitivity of "Middle Atmosphere" Chemistry Configurations of the Community Earth System Model Version 2, Whole Atmosphere Community Climate Model Version 6 (CESM2(WACCM6))

N. A. Davis[1], D. Visioni[2], R. R. Garcia[1], D. E. Kinnison[1], D. R. Marsh[3], M. Mills[1], J. H. Richter[3], S. Tilmes[1], C. G. Bardeen[1], A. Gettelman[4], A. A. Glanville[3], D. G. MacMartin[2], A. K. Smith[1], and F. Vitt[1,5]

[1]Atmospheric Chemistry and Modeling Observations Laboratory, National Center for Atmospheric Research, Boulder, CO, USA, [2]Sibley School of Mechanical and Aerospace Engineering, Cornell University, Ithaca, NY, USA, [3]Climate and Global Dynamics Laboratory, National Center for Atmospheric Research, Boulder, CO, USA, [4]Pacific Northwest National Laboratory, Richland, WA, USA, [5]High Altitude Observatory, National Center for Atmospheric Research, Boulder, CO, USA

Key Points:

- There are differences in stratospheric aerosol optical depth between comprehensive and simplified chemistry configurations
- Simplifying the chemistry scheme generally has smaller global impacts than coarsening the horizontal resolution
- All configurations have similar climate sensitivities and responses to forcings

Supporting Information:

Supporting Information may be found in the online version of this article.

Correspondence to:

N. A. Davis,
ndcodeblue@gmail.com

Citation:

Davis, N. A., Visioni, D., Garcia, R. R., Kinnison, D. E., Marsh, D. R., Mills, M., et al. (2023). Climate, variability, and climate sensitivity of "Middle Atmosphere" chemistry configurations of the Community Earth System Model Version 2, Whole Atmosphere Community Climate Model Version 6 (CESM2(WACCM6)). *Journal of Advances in Modeling Earth Systems*, *15*, e2022MS003579. https://doi.org/10.1029/2022MS003579

Received 12 DEC 2022
Accepted 13 AUG 2023

Author Contributions:

Conceptualization: N. A. Davis, D. Visioni, J. H. Richter, D. G. MacMartin
Data curation: M. Mills, A. A. Glanville
Formal analysis: N. A. Davis, D. Visioni
Investigation: N. A. Davis, D. Visioni
Methodology: N. A. Davis

© 2023 The Authors. Journal of Advances in Modeling Earth Systems published by Wiley Periodicals LLC on behalf of American Geophysical Union. This is an open access article under the terms of the Creative Commons Attribution-NonCommercial License, which permits use, distribution and reproduction in any medium, provided the original work is properly cited and is not used for commercial purposes.

Abstract Simulating whole atmosphere dynamics, chemistry, and physics is computationally expensive. It can require high vertical resolution throughout the middle and upper atmosphere, as well as a comprehensive chemistry and aerosol scheme coupled to radiation physics. An unintentional outcome of the development of one of the most sophisticated and hence computationally expensive model configurations is that it often excludes a broad community of users with limited computational resources. Here, we analyze two configurations of the Community Earth System Model Version 2, Whole Atmosphere Community Climate Model Version 6 (CESM2(WACCM6)) with simplified "middle atmosphere" chemistry at nominal 1 and 2° horizontal resolutions. Using observations, a reanalysis, and direct model comparisons, we find that these configurations generally reproduce the climate, variability, and climate sensitivity of the 1° nominal horizontal resolution configuration with comprehensive chemistry. While the background stratospheric aerosol optical depth is elevated in the middle atmosphere configurations as compared to the comprehensive chemistry configuration, it is comparable among all configurations during volcanic eruptions. For any purposes other than those needing an accurate representation of tropospheric organic chemistry and secondary organic aerosols, these simplified chemistry configurations deliver reliable simulations of the whole atmosphere that require 35% and 86% fewer computational resources at nominal 1 and 2° horizontal resolution, respectively.

Plain Language Summary Modeling the entire atmosphere, or at least from the surface to an altitude of 140 km (87 miles), takes a lot of computer resources. Simulating 1 year can require the equivalent of thousands of personal computers running for 1 day, for example, which is only realistic for researchers with access to a supercomputer. There are many people who would like to simulate the whole atmosphere to study climate change, space weather, and extreme events, but even with access to a supercomputer, it is still computationally expensive to run. We examined a whole atmosphere model with a simpler chemistry scheme, and at a lower horizontal resolution, to see if it still reproduces major features of climate and climate change. The two configurations perform similarly to the high resolution simulation with complex chemistry, with some minor and understandable differences. Anyone looking to simulate the whole atmosphere, using fewer computational resources, can do so confidently using the described model configurations, as long as they are aware of some of the deficiencies.

1. Introduction

Whole atmosphere climate models resolve the interactions between atmospheric dynamics, chemistry, aerosols, and upper atmosphere physics, and are needed to study a wide range of scientific problems. This includes: stratospheric ozone loss (Solomon, 1999; Solomon et al., 1986), its recovery (Fang et al., 2019), and the potential limits of recovery due to future aircraft (J. Zhang et al., 2021) and wildfire emissions (Solomon et al., 2022); geoengineering intended to offset greenhouse gas-induced warming (Kravitz et al., 2015; National Academies of Sciences, Engineering, and Medicine, 2021; Tilmes et al., 2020; Visioni et al., 2021; Weisenstein et al., 2022) and its side effects (Tilmes et al., 2021, 2022; Visioni et al., 2020); sudden stratospheric warming (SSW) impacts on upper

19422466, 2023, 9, Downloaded from https://agupubs.onlinelibrary.wiley.com/doi/10.1029/2022MS003579 by Test, Wiley Online Library on [16/10/2023]. See the Terms and Conditions (https://onlinelibrary.wiley.com/terms-and-conditions) on Wiley Online Library for rules of use; OA articles are governed by the applicable Creative Commons License

Software: D. E. Kinnison, D. R. Marsh, M. Mills, S. Tilmes, C. G. Bardeen, A. Gettelman, A. A. Glanville, A. K. Smith, F. Vitt
Validation: N. A. Davis, D. Visioni
Visualization: N. A. Davis, D. Visioni
Writing – original draft: N. A. Davis, D. Visioni, J. H. Richter, S. Tilmes
Writing – review & editing: N. A. Davis, D. Visioni, R. R. Garcia, D. E. Kinnison, D. R. Marsh, J. H. Richter, S. Tilmes, A. Gettelman, D. G. MacMartin, A. K. Smith

atmosphere variability (Baldwin et al., 2021; Pedatella et al., 2021); space weather (Damiani et al., 2016; Meraner & Schmidt, 2018; Sinnhuber et al., 2012, 2018) and meteor (Plane, 2012) impacts on stratospheric ozone; and the acceleration of the Brewer-Dobson circulation (Abalos et al., 2019, 2021; Chrysanthou et al., 2020; Polvani et al., 2019), its potential impacts on stratospheric (Butchart & Scaife, 2001; Maliniemi et al., 2021) and tropospheric (Neu et al., 2014) ozone, and its implications for global volcanic aerosol transport (Aubry et al., 2021).

These problems have motivated the development of the Community Earth System Model Version 2, Whole Atmosphere Community Climate Model Version 6 (CESM2(WACCM6)), a state of the art fully-coupled whole atmosphere chemistry-climate model with a domain that extends from the surface to the lower thermosphere. The configuration with comprehensive troposphere-stratosphere-mesosphere-lower thermosphere chemistry (Emmons et al., 2020) at nominal 1° horizontal resolution (hereafter "TSMLT") was evaluated by Gettelman, Mills, et al. (2019). However, its computational cost is prohibitive to many researchers and for certain applications, such as long climate integrations. For a given core hour allocation, the research possibilities multiply if nearly-equivalent performance can be achieved by lower core-hour-cost configurations.

While simulating the whole atmosphere requires comprehensive treatments of middle and upper atmosphere physics, including ion chemistry (Verronen et al., 2016) and energetic particle precipitation (Andersson et al., 2016), gravity wave transport (Garcia et al., 2017; Garcia & Solomon, 1985), and molecular diffusion (Chabrillat et al., 2002; Garcia et al., 2014; Smith et al., 2011), the elevated computational cost is primarily due to the inclusion of interactive whole atmosphere chemistry and aerosols. We present here two simpler configurations of CESM2(WACCM6) (Table 1) that make use of the simplified middle atmosphere chemistry scheme, at both nominal 1° and nominal 2° horizontal resolutions (hereafter "MA" and "MA 2°," respectively). These configurations require 35% and 86% fewer computational resources, respectively, compared to the TSMLT configuration at a nominal 1° resolution. The MA scheme neglects non-methane hydrocarbon species and reactions that may otherwise be important for simulating the chemical composition of the troposphere (Kinnison et al., 2007).

Here we describe in detail the climate and variability of the middle and upper atmosphere in these configurations, with a focus on zonal mean temperature and zonal mean zonal wind, SSWs, the Quasi-Biennial Oscillation (QBO), tropical stratospheric upwelling, stratospheric ozone and aerosols, and the tropical tape recorder, as well as several measures of surface climate, including global mean surface temperature, Arctic sea ice, and climate sensitivity. We show that many aspects of surface climate and middle atmospheric climate and variability are similar in these lower-cost configurations. With a few caveats, they can be used in studies that do not require all of the complexities of the comprehensive TSMLT configuration.

2. Model Configurations

Our analysis focuses on configurations of CESM2(WACCM6) that use the finite volume dynamical core (Lin & Rood, 1997), with 70 vertical levels from the surface to 4.5×10^{-6} hPa—approximately 140 km altitude. The finite volume dynamical core is run at either a 1° nominal (0.95° × 1.25°) or 2° nominal (1.95° × 2.25°) horizontal resolution.

CESM2(WACCM6) inherits the physics of the low-top Community Atmosphere Model Version 6.0, including: Zhang-McFarlane deep convection (G. J. Zhang & McFarlane, 1995); Cloud Layers Unified By Binormals (Golaz et al., 2002; Larson, 2017), a unified turbulence and cloud scheme; Morrison-Gettelman Version 2 microphysics (Gettelman & Morrison, 2015); subgrid orographic drag (Beljaars et al., 2004); an orographic gravity wave scheme based on Scinocca and McFarlane (2000); the Rapid Radiative Transfer Model for General circulation models radiation (Iacono et al., 2008; Mlawer et al., 1997); and the Modal Aerosol Model Version 4 (Liu et al., 2016; Mills et al., 2016).

In addition to these shared physics schemes, CESM2(WACCM6) also includes convectively- and frontally-generated gravity wave schemes (Richter et al., 2010), molecular diffusion (Garcia et al., 2007), resolved gas-phase and aerosol chemistry, and photoionization, photodissociation, and photoelectron production by solar and geomagnetic forcings. The TSMLT (Emmons et al., 2020; Gettelman, Mills, et al., 2019) and MA (Kinnison et al., 2007) chemical mechanisms model the extended O_x, NO_x, HO_x, ClO_x, and BrO_x chemical families, CH_4 and its degradation products, N_2O, H_2O, CO_2, CO, and ClO_x and BrO_x precursors (see Emmons et al. (2020) for a full description of each chemical family). The TSMLT mechanism also models nonmethane hydrocarbons, oxygenated organics, two very short-lived halogens, and secondary organic aerosols (SOA) via the volatility basis set approach (Hodzic

19422466, 2023, 9, Downloaded from https://agupubs.onlinelibrary.wiley.com/doi/10.1029/2022MS003579 by Test, Wiley Online Library on [16/10/2023]. See the Terms and Conditions (https://onlinelibrary.wiley.com/terms-and-conditions) on Wiley Online Library for rules of use; OA articles are governed by the applicable Creative Commons License

Table 1
Approximate Number of Central Processor Unit Core Hours Needed to Complete One Simulated Year of the Specified Configuration of CESM2(WACCM6), and Approximate Number of Simulated Years per Day

Configuration	Core hours	Throughput (sim. year/day)
1 deg., TSMLT	19,900	4.3
1 deg., MA	12,800	6.7
2 deg., MA	2,700	5.1

Note. All configurations assume interactive ocean, sea ice, and land model components. A core hour is the computational resource of running one CPU for 1 hr. 1° configurations were run with 3,564 cores, while the 2° configuration was run with 576 cores due to the inherent scaling limit of the finite volume dynamical core. Based on simulations performed on NCAR's Cheyenne supercomputer.

et al., 2016; Tilmes et al., 2019). The TSMLT mechanism includes a total of 231 species, 403 gas-phase reactions, and 30 heterogeneous reactions, while the MA mechanism includes a total of 59 species, 217 gas-phase reactions, and 17 heterogeneous reactions.

Surface area density derived from MAM4 is used to drive heterogeneous chemistry (Mills et al., 2016). Tropospheric heterogeneous reactions consider sulfate, black carbon, particulate organic matter, and secondary organic aerosol, while stratospheric heterogeneous reactions consider sulfate, nitric acid trihydrate, and water-ice (Gettelman, Mills, et al., 2019; Mills et al., 2016, 2017). A more complete description of the chemistry and aerosol suite can be found in Section 2.4 of Gettelman, Mills, et al. (2019).

WACCM6 is coupled to the Parallel Ocean Program Version 2 (POP2) (Danabasoglu et al., 2012), the Community Ice CodE Version 5 (CICE5) (Hunke et al., 2015), the Community Land Model Version 5 (CLM5) (Lawrence et al., 2019), and the Model for Scale Adaptive River Transport (MOSART) (Li et al., 2013) via the Community Infrastructure for Modeling Earth coupler (Danabasoglu et al., 2020). POP2 is a comprehensive ocean model discretized onto 60 vertical levels and a "Greenland pole" horizontal mesh. POP2 includes parameterized ocean biogeochemistry. CICE5, a prognostic sea ice model, shares the same horizontal grid as POP2. Soil and vegetation dynamics and land surface biogeochemistry are modeled with CLM5, while river transport is modeled with MOSART.

Surface mixing ratios of greenhouse gases are specified as in Meinshausen et al. (2017), while anthropogenic (Hoesly et al., 2017, 2018) and biomass burning (van Marle et al., 2016, 2017) emissions of reactive gases and aerosols are released in the lowest model level. Biogenic emissions from CLM5 (Guenther et al., 2012) and NO_x production by lightning (Price et al., 1997) are interactive and computed online. Volcanic emissions of SO_2 are prescribed from Volcanic Emissions for Earth System Models (Neely & Schmidt, 2016) with modifications described in Mills et al. (2016).

The QBO is driven spontaneously by a mix of resolved tropical waves and parameterized gravity wave drag in both 1° configurations of the model. The 70 vertical levels in these simulations are insufficient to accurately resolve wave dissipation and the descent of the QBO, though this can be ameliorated by increasing the number of vertical levels to 110 (Garcia & Richter, 2019). However, the tropical zonal winds are nudged to idealized observations between 4 and 86 hPa and 10°S to 10°N in the MA 2° configuration (Matthes et al., 2010) as it was not tuned to have a spontaneous QBO.

We conducted three Coupled Model Intercomparison Project Phase 6 (CMIP6) experiments: three Historical (HIST) simulation ensemble members, from 1850 to 2014; one preindustrial control (piControl) simulation from arbitrary years 0–1,000; and one abrupt quadrupling of CO_2 ($4xCO_2$) simulation from arbitrary years 0–150 (Eyring et al., 2016), for each configuration. While 150 years is sufficient to obtain an estimate of climate sensitivity, it is likely to be an underestimate (Rugenstein et al., 2020). We also conducted one SSP2-4.5 simulation for the TSMLT and MA configurations to evaluate the chemical mechanisms' stratospheric ozone recovery. All simulations are fully coupled, with prognostic ocean, sea ice, land, and river runoff components.

3. Evaluation Data Sets

We evaluate the zonal mean climate of the whole atmosphere using a combination of the National Aeronautics and Space Administration (NASA) Modern Era Retrospective Reanalysis version 2 (MERRA2; Gelaro et al., 2017) output and NASA Sounding of the Atmosphere using Broadband Radiometry version 2.0 (SABER; Dawkins et al., 2018; Remsberg et al., 2008) retrievals, in addition to NASA Microwave Limb Sounder (MLS; Lambert et al., 2007) version 4.2 and NASA Solar Backscatter Ultraviolet (SBUV; McPeters et al., 2013) satellite retrievals.

MERRA2 is a reanalysis that assimilates in-situ and remotely-sensed observations of the atmosphere to produce a highly-constrained reconstruction of atmospheric variability from 1980 to the present. Here we use temperature and zonal wind output from the assimilation product through 2014 (Global Modeling and Assimilation

19422466, 2023, 9, Downloaded from https://agupubs.onlinelibrary.wiley.com/doi/10.1029/2022MS003579 by Test, Wiley Online Library on [16/10/2023]. See the Terms and Conditions (https://onlinelibrary.wiley.com/terms-and-conditions) on Wiley Online Library for rules of use; OA articles are governed by the applicable Creative Commons License

Office, 2015). SABER, an instrument onboard the NASA Thermosphere Ionosphere Mesosphere Energetics and Dynamics satellite, makes limb measurements of CO_2, O_3, and H_2O infrared emissions, with temperature and geopotential height retrievals available between approximately 100 and 0.0001 hPa.

While MERRA2 has a model lid at 0.01 hPa (Molod et al., 2015), its sponge layer begins at 0.24 hPa (Fujiwara et al., 2017). For this reason, we create a combined "MERRA2 & SABER" evaluation data set that combines MERRA2 from the surface to 0.24 hPa, and SABER from 0.24 to 0.0001 hPa. In zonal mean plots, we leave the altitude regions between 0.24 hPa and 0.1 hPa shaded gray to note this transition. SABER only has continuous coverage between 53°S and 53°N (Randel et al., 2016), so we exclude all SABER retrievals poleward of 53° and similarly shade them gray. For SABER, daily average temperature and geopotential height from the version 2.0 retrievals (GATS, Inc, 2015) are gridded by interpolating each profile to a common pressure grid and then averaging into 1° zonal mean bins. Daily mean zonal winds are derived from gridded SABER geopotential height through geostrophic balance. Monthly means are constructed by averaging these daily means.

MLS version 4.2 retrievals (Lambert et al., 2015) of water vapor are used as an evaluation data set for the stratospheric tape recorder (Mote et al., 1996). MLS is situated onboard NASA's Earth Observing System Aura satellite and measures microwave emissions from the atmospheric limb. As in Glanville and Birner (2017), daily profiles of water vapor are averaged between 10°S and 10°N to produce daily average stratospheric water vapor, from which monthly averages are constructed. There is some evidence of a drift in MLS version 4 retrievals (Livesey et al., 2021), but they begin near the end of our analysis period and are substantially smaller than the biases examined here.

We use SBUV Version 8.6 merged ozone retrievals (Goddard Space Flight Center, 2022) to evaluate polar stratospheric ozone (Frith et al., 2014). The merged data set is constructed from ozone retrievals from nine satellites from 1970 to the present, including the Nimbus-4 BUV, Nimbus-7 SBUV, and NOAA SBUV/2 instruments. Except for Nimbus-4, there is overlap among the different missions which allows for a more direct calibration. As there was an approximately 2 years gap between Nimbus-4 and Nimbus-7, there is additional uncertainty for retrievals from 1970 to 1972. We do not use the retrievals from Nimbus 4 after 1972, as there is limited coverage.

Global mean surface temperatures are evaluated with two observational data sets: Goddard Institute for Space Studies Surface Temperature version 4 (GISSTEMPv4; Lenssen et al., 2019; GISTEMP Team, 2022) and Hadley Center/Climatic Research Unit Temperature version 5 (HadCRUT5; Climatic Research Unit (University of East Anglia) and Met Office, 2022; Morice et al., 2012). Both data sets combine observations of sea surface temperatures and air temperatures over land, with slightly different homogenization and hole-filling methods. We also evaluate Arctic sea ice with two observational data sets: sea ice area derived from the National Snow and Ice Data Center Sea Ice Index version 3 (NSIDC; Fetterer et al., 2017), and sea ice volume from the Pan-Arctic Ice Ocean Modeling and Assimilation System (PIOMAS; Schweiger et al., 2011). NSIDC is a fully observational product derived from passive microwave satellite measurements, while PIOMAS sea ice volume is derived from a sea ice model that assimilates satellite and in situ measurements (J. Zhang & Rothrock, 2003).

4. Methods and Definitions

Following the World Meteorological Organization, the tropopause is defined as the first level at which the tropospheric lapse rate decreases to 2 K km^{-1}, provided it remains below 2 K km^{-1} between that level and all levels within 2 km above. We define the stratopause as the warmest level between the tropopause and 0.01 hPa, and the mesopause as the coldest level above the stratopause. The "pauses" are evaluated with monthly mean, zonal mean output.

SSWs are identified as in Charlton and Polvani (2007), which classifies the central date of an SSW as the date when the daily average zonal mean zonal wind at 10 hPa and 60°N becomes easterly from November through March. After an SSW is identified, subsequent events are identified only if the central date occurs after more than 20 days of consecutive westerlies after the central date of the preceding event.

Tropical stratospheric upwelling, M, is defined as the area average of all transformed Eulerian mean (TEM) upward motion at each vertical level,

$$M(p) = \frac{\sum_{-90}^{90}[w^*](p,\phi)\delta(p,\phi)\cos(\phi)}{\sum_{-90}^{90}\delta(p,\phi)\cos(\phi)} \quad (1)$$

19422466, 2023, 9, Downloaded from https://agupubs.onlinelibrary.wiley.com/doi/10.1029/2022MS003579 by Test, Wiley Online Library on [16/10/2023]. See the Terms and Conditions (https://onlinelibrary.wiley.com/terms-and-conditions) on Wiley Online Library for rules of use; OA articles are governed by the applicable Creative Commons License

where p is the pressure, ϕ is the latitude, $[w^*]$ is the TEM residual vertical velocity, defined by

$$\left[w^*\right] = [w] + \frac{1}{a}\frac{\partial}{\partial\phi}\frac{\left[v'\theta'\right]}{\partial[\theta]/\partial p} \tag{2}$$

where w is the vertical wind, a is the radius of the Earth, θ is the potential temperature, brackets indicate the zonal mean, and primes indicate zonal deviations, and $\delta(p, \phi)$ is equal to 1 for positive $[w^*]$ and 0 otherwise.

Climate sensitivity to a doubling of CO_2 is evaluated with the $4xCO_2$ experiment through the method detailed in Gregory et al. (2004). Annual mean top-of-atmosphere net downward radiative flux, F_{TOA}, is regressed on the annual mean global mean surface temperature anomaly, T_{anom}, producing slope a and intercept b:

$$F_{TOA} = aT_{anom} + b \tag{3}$$

T_{anom} is the difference between the global mean surface temperature and the time-mean global mean surface temperature from the final 100 years of the piControl simulation. The global mean surface temperature anomaly corresponding to a top-of-atmosphere net downward radiative flux of zero is considered the balanced response, or equilibrium climate sensitivity (ECS), and is calculated directly as

$$ECS = -\frac{1}{2}\frac{b}{a} \tag{4}$$

with the factor of 1/2 because this is inferred from the $4xCO_2$ experiment.

We derive a power spectral density-weighted period to objectively assess the period of the QBO. A Fourier transform is applied to the daily zonal mean zonal wind averaged between 10°S and 10°N at each vertical level, and the period of the QBO, T_{QBO}, is estimated by weighting all periods by their power spectral density,

$$T_{QBO} = \frac{\sum_{n=1}^{N} P(n)/f(n)}{\sum_{n=1}^{N} P(n)} \tag{5}$$

where f is the frequency in month^{-1}, P is the power spectral density, and the sum is taken over all frequencies from $n = 1$ to N, where N is the frequency with period equal to half of the length of the time series. This summation excludes the mean, which has an infinite period.

As in Dunkerton and Delisi (1985), the QBO amplitude is estimated from the standard deviation of the climatological anomalies in the zonal mean zonal wind averaged between 10°S and 10°N.

Age of air is a hypothetical measure of the residence time of air within the stratosphere that captures the sum total of all transport processes (Waugh & Hall, 2002). Here we assess age of air with the artificial AOA1 tracer, which has no sinks but a linearly-increasing upward flux at the lower boundary, in contrast to Garcia et al. (2011) which used a linearly-increasing specified lower boundary condition. For each grid point, and at each time step, the age of air is defined as the time interval between the current time and the time AOA1 reached its present value but at the reference latitude and pressure. We apply a 12-month running mean to AOA1 before calculating the age of air, and set the reference latitude and pressure to 0.1°N and 100 hPa, respectively.

5. Preindustrial Control Climate

We begin with a brief survey of some global mean parameters in the piControl climates, displayed in Table 2, including: shortwave, longwave, and total cloud radiative effects, global mean precipitation, global mean surface temperature, and the top-of-model net radiative imbalance. The configurations all have statistically indistinguishable top-of-model net radiative imbalances, and the shortwave and total cloud radiative effects and global mean precipitation are indistinguishable between the TSMLT and MA configurations. In all other cases, the global mean variables in both MA and MA 2° are statistically significantly different from the TSMLT configuration. In the MA 2° configuration, the shortwave and longwave cloud radiative effects are weaker, the precipitation rate is higher, and the surface temperature is warmer than in TSMLT and MA. In the MA configuration the differences are the opposite and generally smaller, with slightly stronger cloud radiative effects and a cooler surface temperature than TSMLT. Curiously, MA 2° has both the highest global mean surface temperature and highest total cloud

19422466, 2023, 9, Downloaded from https://agupubs.onlinelibrary.wiley.com/doi/10.1029/2022MS003579 by Test, Wiley Online Library on [16/10/2023]. See the Terms and Conditions (https://onlinelibrary.wiley.com/terms-and-conditions) on Wiley Online Library for rules of use; OA articles are governed by the applicable Creative Commons License

Table 2
Global Mean Values of Key Variables Derived From Monthly Mean Output From the Last 100 Years of Each piControl Simulation

	1 deg., TSMLT	1 deg., MA	2 deg., MA
Shortwave cloud radiative effect	-48.3 ± 0.4 W m^{-2}	-48.8 ± 0.4 W m^{-2}	$-46.7^{\dagger\ddagger} \pm 0.4$ W m^{-2}
Longwave cloud radiative effect	25.3 ± 0.1 W m^{-2}	$25.7^{\dagger} \pm 0.1$ W m^{-2}	$22.8^{\dagger\ddagger} \pm 0.1$ W m^{-2}
Total cloud radiative effect	-23.0 ± 0.5 W m^{-2}	-23.1 ± 0.5 W m^{-2}	$-23.9^{\dagger\ddagger} \pm 0.4$ W m^{-2}
Precipitation	2.9 ± 0.1 mm/day	2.9 ± 0.1 mm/day	$3.0^{\dagger\ddagger} \pm 0.1$ mm/day
Surface temperature	287.1 ± 0.1 K	$286.9^{\dagger} \pm 0.1$ K	$287.3^{\dagger\ddagger} \pm 0.1$ K
Top-of-model net radiative imbalance	0.1 ± 0.7 W m^{-2}	0.0 ± 0.7 W m^{-2}	0.1 ± 0.7 W m^{-2}

Note. 95% confidence intervals assume 1 degree of freedom per season. Daggers indicate the value in the MA or MA 2° configuration is statistically significantly different from its value in the TSMLT configuration at the 95% confidence level, based on a two-sided *t*-test for the difference of means, assuming 1 degree of freedom per year. Double daggers indicate the same, but for the difference between the values in the MA and MA 2° configurations.

radiative effect, which may indicate that the cloud radiative effect is not responsible for the difference in global mean surface temperature. Overall, horizontal resolution impacts some aspects of the global mean climate more than the chemistry scheme. However, the differences among these configurations are generally smaller than the differences between WACCM6 and WACCM4 (Gettelman, Mills, et al., 2019).

6. Zonal Mean Climate and Variability

A comparison of zonal mean temperatures for December–January–February and June–July–August is shown in Figure 1. In this section we exclusively analyze the historical simulations, and average over all ensemble members except where noted. The middle and upper atmosphere exhibit a strong seasonality in temperature, with a markedly warmer stratosphere and colder mesosphere, as well as lower stratopause and mesopause, in local summer (Figures 1a, 1b, 1f, and 1g). We note that MERRA2 zonal mean temperatures are comparable to other modern reanalyzes and observations, except in the upper stratosphere where it exhibits some large (greater than 2 K) biases (Long et al., 2017).

The TSMLT configuration (Figures 1b and 1g) largely reflects the seasonality observed in MERRA2 & SABER. However, in the tropics TSMLT is 6 K warmer just above the stratopause and 15 K warmer below the mesopause (Figures 1c and 1h). It is also up to 15 K warmer in the upper polar stratosphere in winter, and up to 15 K cooler in the Southern hemisphere stratosphere in austral summer. Additionally, the location of the minimum temperature in the summer mesosphere is slightly lower in altitude in the TSMLT configuration, such that the mesopause drops off in altitude more sharply with latitude than observed in the subtropics.

Simplifying the chemistry scheme has no impact on these temperature biases throughout almost all of the domain, even in the troposphere where the impact on chemical climate would be the largest (Figures 1d and 1i). There is only a 3 K decrease in temperature above the mesopause in the Southern hemisphere in December-January-February (DJF) (Figure 1d).

However, the zonal mean temperature in MA 2° is up to 24 K colder than in TSMLT above the summer mesopause in the lower thermosphere (Figures 1e and 1j). The dipole around the summer mesopause indicates the mesopause is higher in altitude in MA 2° than in TSMLT, which corrects some of the bias in TSMLT relative to SABER. This could be due to slight differences in the parameterized gravity wave drag at coarser resolution (see Figure S1 in Supporting Information S1). The winter polar mesosphere and lower thermosphere is 3 K warmer in MA 2° than in TSMLT, but given SABER's limited coverage, it isn't clear whether this is an improvement.

While the zonal mean surface zonal wind is set by the column-integrated momentum stress, the vertical shear in the zonal mean zonal wind at any given level is proportional to the vertically-integrated meridional temperature gradient below. In the troposphere, the symmetric equator-to-pole temperature gradient is associated with westerly jets in each hemisphere (Figures 2a, 2b, 2f, and 2g), which rapidly taper off into the lower stratosphere with the reversal of the equator-to-pole temperature gradient.

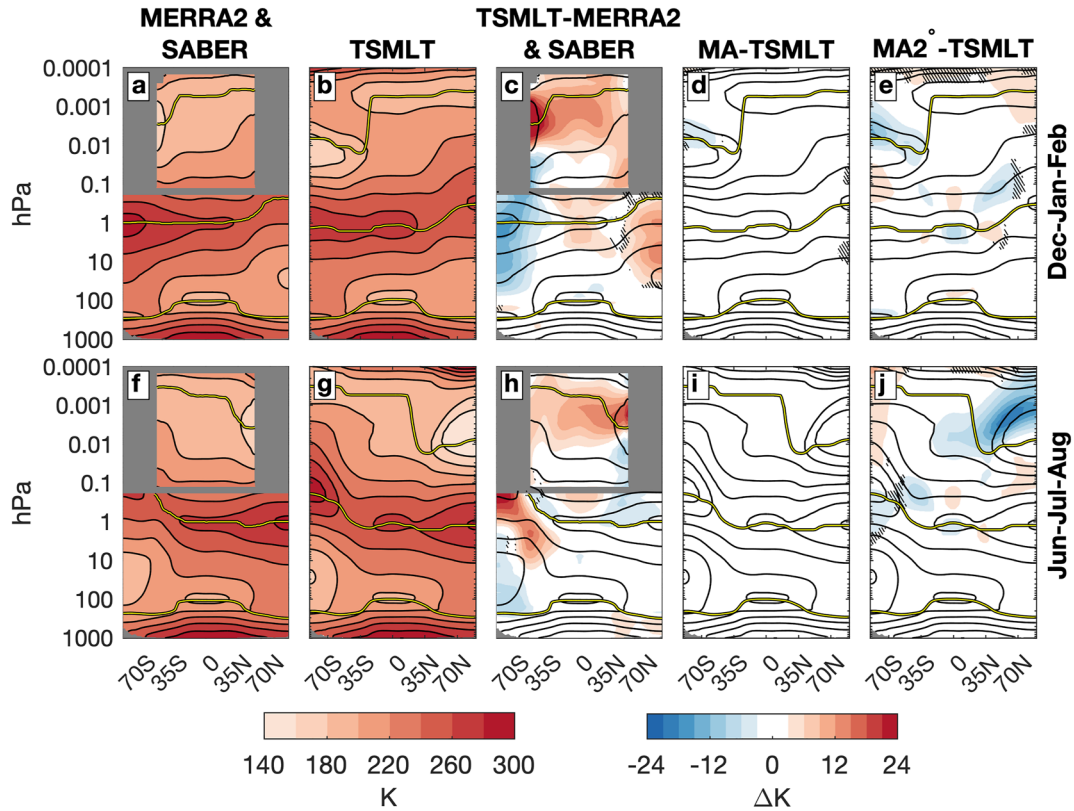

Figure 1. 1980–2015 average zonal mean temperature in (first column) Modern Era Retrospective Reanalysis version 2 (MERRA2) & Sounding of the Atmosphere using Broadband Radiometry (SABER), (second column) tropospher e-stratosphere-mesosphere-lower thermosphere (TSMLT), and difference in zonal mean temperature between (third column) TSMLT and MERRA2 & SABER, (fourth column) middle atmosphere (MA) and TSMLT, and (fifth column) MA 2° and TSMLT, for both (top row) December–January–February and (bottom row) June–July–August. Climatology is color shaded every 20 K in (a), (b), (f), and (g); while differences are shaded every 3 K in (c), (d), (e), (h), (i), and (j). The MERRA2 & SABER climatology is contoured in (c) and (h) and the TSMLT climatology is contoured in (d), (e), (i), and (j). Values not statistically significantly different at the 95% confidence level are hatched, but only where there is shading. The tropopause, stratopause, and mesopause are shown by the yellow contours. All model results are from the historical simulations.

On a global scale, however, the meridional temperature gradient of the stratosphere is primarily pole-to-pole. Accordingly, both the winter westerly and summer easterly stratospheric/mesospheric jet core is situated near the stratopause, where the pole-to-pole temperature gradient changes sign (Figures 2a, 2b, 2f, and 2g). Above the stratopause, the pole-to-pole temperature gradient maintains its sign through the mesosphere and into the lower thermosphere, associated with the winter easterly and summer westerly thermospheric jets.

In TSMLT a westerly stratospheric/mesospheric jet up to 20 m s^{-1} weaker than in MERRA2 (Figures 2c and 2h) is associated with a warmer pole (Figures 1c and 1h), while a westerly thermospheric jet up to 40 m s^{-1} stronger than in SABER is associated with the warmer equator. As is the case for the zonal mean temperature, there is no material impact from simplifying the chemistry scheme (Figures 2d and 2i). In MA 2°, minor temperature differences in the tropical mesosphere (Figures 1e and 1j) are associated with 20–30 m s^{-1} differences in the tropical zonal mean zonal winds (Figures 2e and 2j). These differences are tilted toward the summer thermosphere, where the mesopause is higher in MA 2° than in TSMLT, and have mixed impacts on the biases in the lower thermosphere (Figures 2c and 2h). The differences among the model configurations are generally smaller than the model biases relative to MERRA2 & SABER, however.

The climate and variability of the Northern and Southern hemisphere stratospheric polar vortices are similarly consistent among the different configurations (Figure 3). In the Northern hemisphere, the vortex strength exhibits increased variability in winter due to wave forcing, while in the Southern hemisphere, the greatest variability occurs in spring. From November through April, the distributions of daily Northern hemisphere polar

19422466, 2023, 9, Downloaded from https://agupubs.onlinelibrary.wiley.com/doi/10.1029/2022MS003579 by Test, Wiley Online Library on [16/10/2023]. See the Terms and Conditions (https://onlinelibrary.wiley.com/terms-and-conditions) on Wiley Online Library for rules of use; OA articles are governed by the applicable Creative Commons License

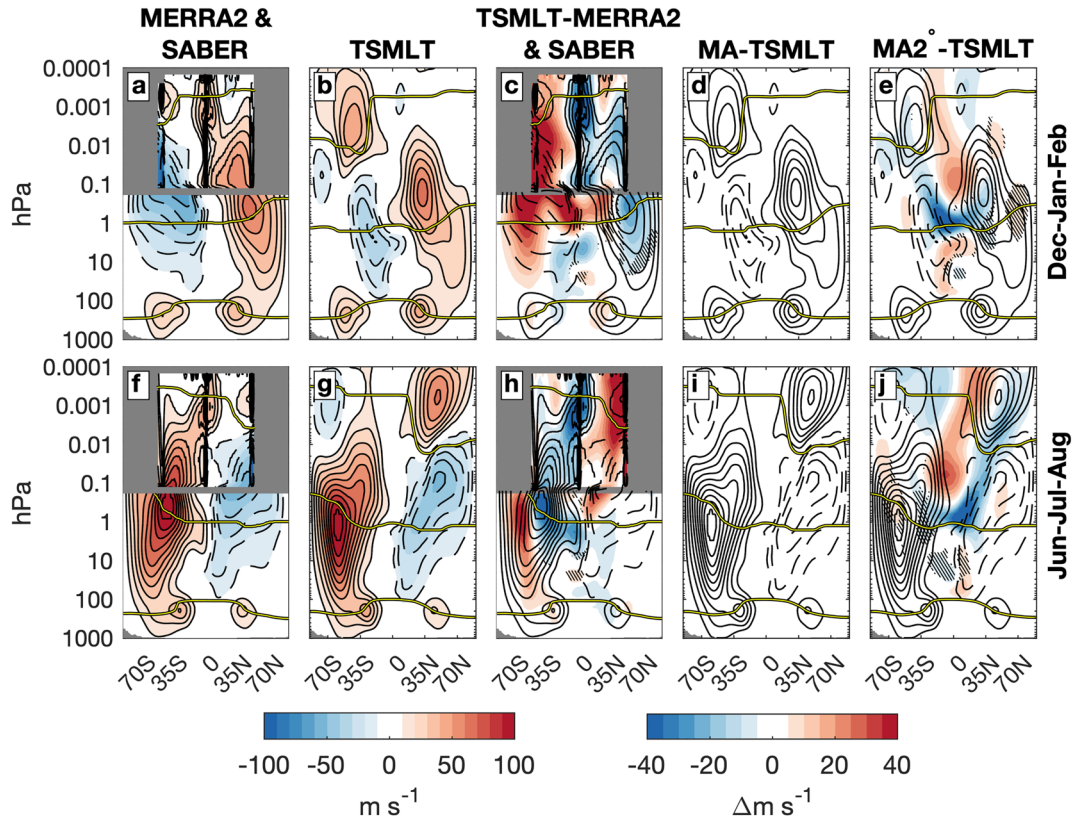

Figure 2. As in Figure 1, but for the zonal mean zonal wind, with climatology shaded every 10 m s^{-1} and differences shaded every 5 m s^{-1}.

vortex strength in all configurations of WACCM6 are statistically significantly different from the distributions in MERRA2 (Figures 3a–3c). The distributions in WACCM6 are narrower, due to both lower maximum and higher minimum daily zonal wind values. In the Southern hemisphere, the vortex in WACCM6 is significantly stronger throughout the seasonal cycle (Figures 3d–3f). Only one (major) SSW has been observed in the Southern hemisphere over the reanalysis era, but none are simulated in WACCM6.

SSWs occur on average every 2 years in the Northern hemisphere from December through March, with statistically equal frequency in December through March (Figure 4), though there visually appear to be more in January and February. All WACCM6 ensemble members simulate at least one November SSW, but of these, only 2 members are statistically significantly different from the frequency of 0 in MERRA2. Here, we estimate the monthly 95% confidence intervals using a binomial distribution based on $N = 25$ yearly samples. For a binomial distribution to be valid, we must assume that only one SSW occurs in a given month in a given year (which is never violated). These early winter SSWs in WACCM6 can be seen in the vortex statistics, where the minimum wind line becomes negative approximately 1 month before MERRA2 (Figures 3a–3c). Apart from these November SSWs, there are some MA ensemble members that simulate too few SSWs relative to MERRA2 in February. Overall, though, we do not find that the SSW frequencies in any of the WACCM6 configurations are consistently biased relative to the observed frequencies at a statistically significant level.

In the tropical stratosphere, the dominant mode of variability is the QBO (Baldwin et al., 2001), which has wide-ranging impacts on global teleconnections (Scaife et al., 2014; Toms et al., 2020). The dissipation of upward-propagating gravity, Kelvin, and mixed Rossby-gravity waves in the stratosphere drives the downward propagation of each phase of the QBO (Garcia & Richter, 2019; Holt et al., 2022), producing its characteristic 28-month period (Figures 5a and 5b). In WACCM6, the spontaneously-generated QBO in TSMLT and MA has a slightly shorter period than in MERRA2 throughout the middle and upper stratosphere (Figures 5d, 5e, 5g, 5h). Further, the wind anomalies are weaker than those in MERRA2—which can be seen in the weaker QBO amplitude (Figures 5f and 5i)—and they do not descend below 50 hPa (Figures 5d and 5g). Instead, the tropical

19422466, 2023, 9, Downloaded from https://agupubs.onlinelibrary.wiley.com/doi/10.1029/2022MS003579 by Test, Wiley Online Library on [16/10/2023]. See the Terms and Conditions (https://onlinelibrary.wiley.com/terms-and-conditions) on Wiley Online Library for rules of use; OA articles are governed by the applicable Creative Commons License

19422466, 2023, 9, Downloaded from https://agupubs.onlinelibrary.wiley.com/doi/10.1029/2022MS003579 by Test, Wiley Online Library on [16/10/2023]. See the Terms and Conditions (https://onlinelibrary.wiley.com/terms-and-conditions) on Wiley Online Library for rules of use; OA articles are governed by the applicable Creative Commons License

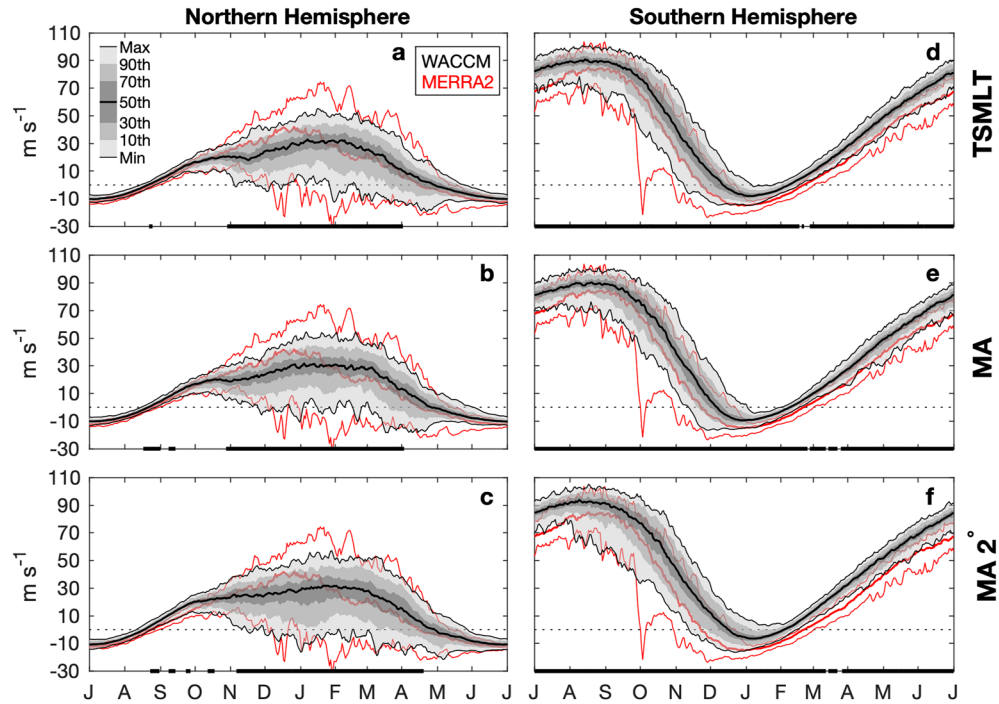

Figure 3. Stratospheric polar vortex strength assessed from the zonal mean zonal wind at 60° and 10 hPa for the (left column) Northern and (right column) Southern hemisphere, in (top row) troposphere-stratosphere-mesosphere-lower thermosphere (TSMLT), (middle row) middle atmosphere (MA), and (bottom row) MA 2°. WACCM6 statistics shown by black lines and shading, while the Modern Era Retrospective Reanalysis version 2 (MERRA2) minimum, maximum, and median are shown by the red lines. Differences in the vortex strength distribution that are statistically significantly different at the 95% confidence level are shown by the black line along the date axis. The polar vortex is defined as the zonal mean zonal wind at 60° latitude and 10 hPa. All model results are from the historical simulations.

lower stratosphere has steady westerly winds. The QBO in MA 2° is highly correlated with the observed QBO in MERRA2 because it is nudged (Figures 5j–5l). However, some higher-frequency variability visible in MERRA2 (Figure 5a) is missing in MA 2° (Figure 5j).

Upwelling by the wave-driven residual circulation in the tropics is one of the key pathways through which tracers enter the stratosphere. Both the TSMLT and MA configurations have stronger climatological stratospheric upwelling than MERRA2 below 60 hPa, whereas MA 2° has significantly stronger upwelling than MERRA2 above 80 hPa (Figure 6a). This may be due to an apparent upward shift of the upwelling profile in the 1° configurations relative to both MERRA2 and the MA 2° configuration. Over the historical period, MERRA2 exhibits a statistically significant and consistent 5%/decade acceleration of upwelling at all levels. While the upwelling trends in the WACCM6 configurations are approximately 50% weaker and only significant below 30 hPa, they are consistent with one another.

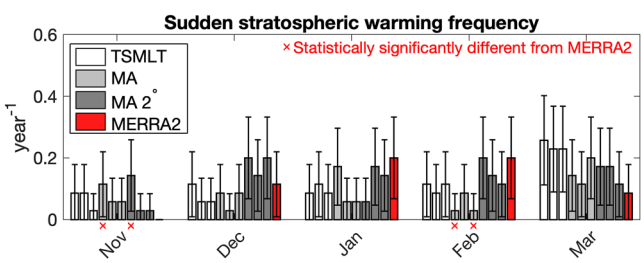

Figure 4. Northern hemisphere sudden stratospheric warming frequency in each ensemble member and in Modern Era Retrospective Reanalysis version 2 (MERRA2). 95% confidence intervals are shown as whiskers, while a red x indicates an ensemble member has a frequency statistically significantly different from MERRA2 at the 95% confidence level based on a binomial distribution. All model results are from the historical simulations.

The residual circulation is only the advective component of the Brewer-Dobson circulation. The other component—horizontal and vertical mixing by eddies—can drive apparent vertical transport in the tropics (Glanville & Birner, 2017). The mixing ratio of water vapor at the tropical tropopause has a seasonal cycle and is quasi-conserved during ascent, excepting the source from methane oxidation, giving rise to the water vapor tape recorder (Figures 7a and 7b; Mote et al., 1996). Below 70 hPa, both the TSMLT and MA 2° configurations have a pronounced dry bias relative to MLS in boreal summer. Above 70 hPa, the 1° configurations are up to 0.5 ppm drier in and above the dry part of the signal (around 3.25–3.5 ppm), and up to 0.5 ppm wetter in and above the wet part of the signal (around 4 ppm;

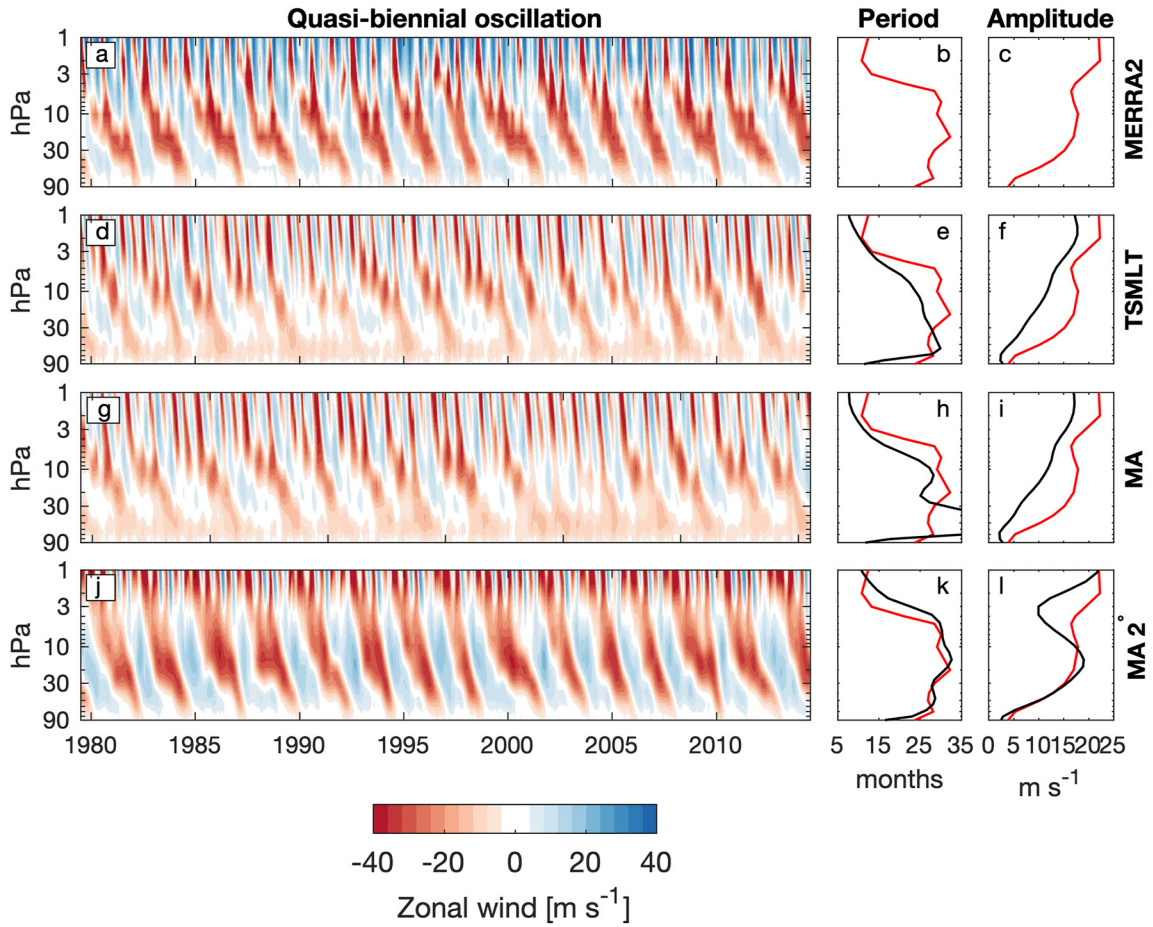

Figure 5. Daily mean zonal mean zonal wind averaged from 10°S to 10°N from (a) Modern Era Retrospective Reanalysis version 2 (MERRA2) and (d, g, j) the second ensemble member of each configuration of Whole Atmosphere Community Climate Model Version 6, shaded every 4 m s^{-1}, (b, e, h, k) the power-weighted period of the zonal mean zonal wind, and (c, f, i, l) the Quasi-Biennial Oscillation amplitude, with MERRA2 displayed in red. All model results are from the historical simulations.

Figures 7c and 7d). This dipole indicates stronger net ascent, with the dry signal reaching 25 hPa (Figure 7b) rather than 35 hPa (Figure 7a) within one year. On the other hand, MA 2° is significantly wetter than MLS throughout most of the dry part of the signal (Figure 7e).

Age of air provides a more global perspective of stratospheric transport (Figure 8). In the stratosphere the air is youngest at the tropopause and reaches a maximum of nearly 5 years in the polar upper stratosphere (Figure 8a). Age of air in the MA configuration is approximately 3 months younger throughout the stratosphere, with a maximum difference of 1 year near the Northern hemisphere subtropical jet (Figure 8b). On the other hand, the age of air in the lower stratosphere in the MA 2° configuration is up to 6 months older, and oriented approximately parallel with midlatitude isentropic eddy mixing.

In the subtropical lower stratosphere, stronger mixing tends to increase the age-of-air by injecting older extratropical air into the fresh air of the tropical pipe. Due to methane oxidation, stratospheric water vapor tends to increase away from the tropical pipe, such that mixing acts to moisten the tape recorder. A reasonable hypothesis is that the MA 2° configuration may have stronger mixing in the subtropical lower stratosphere, which leads to locally-enhanced age-of-air (Figure 8c) and a wetter tape recorder throughout the year (Figure 7e).

7. Historical Climate Change and Climate Sensitivity

An important question is whether simplified chemistry or horizontal resolution impact climate sensitivity. While the different configurations have statistically significantly different absolute global mean surface temperatures

19422466, 2023, 9, Downloaded from https://agupubs.onlinelibrary.wiley.com/doi/10.1029/2022MS003579 by Test, Wiley Online Library on [16/10/2023]. See the Terms and Conditions (https://onlinelibrary.wiley.com/terms-and-conditions) on Wiley Online Library for rules of use; OA articles are governed by the applicable Creative Commons License

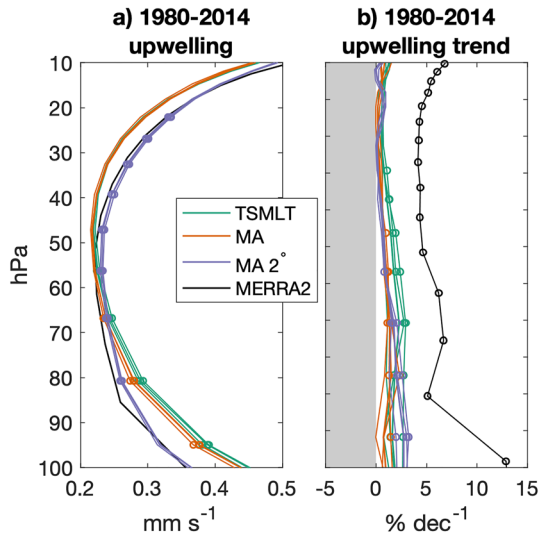

Figure 6. 1980–2014 tropical stratospheric upwelling (a) mean and (b) trend. Circles in (a) denote values statistically significantly different from Modern Era Retrospective Reanalysis version 2 (MERRA2) at the 95% confidence level, while circles in (b) denote trends statistically significant at the 95% confidence level. All model results are from the historical simulations.

(Figures 9a and 9b)—with MA cooler than TSMLT by 0.2 K but MA 2° warmer than TSMLT by 0.3 K, consistent with their piControl climates (Table 2)—their 1980–2014 trends are similar, ranging from just over 0.2 K dec^{-1} to 0.35 K dec^{-1} (Figures 9c and 9d). All WACCM6 ensemble members have global mean surface temperature trends statistically significantly larger than both HadCRUT5 and GISSTEMPv4, which is consistent with the known higher climate sensitivity of CESM2 (Gettelman, Hannay, et al., 2019).

This enhanced response to forcings is reflected in Northern hemisphere sea ice trends, as well (Figure 10). September Arctic sea ice area trends are statistically significantly stronger than observed across WACCM6 configurations, with the lone exception being one MA ensemble member (Figures 10a and 10b). Similarly, trends in annual mean Arctic sea ice volume are statistically significantly stronger in all TSMLT and MA 2° ensemble members than in observations (Figures 10c and 10d). Only one of three MA ensemble members has an annual mean Arctic sea ice volume trend statistically significantly stronger than observed. These more negative trends are partially related to the more abundant sea ice in WACCM6 in the 1980s than was observed (Figures 10a and 10c).

The historical simulations include a multitude of anthropogenic and natural forcings. Isolating the cause of these differences—both across ensemble members and between WACCM6 and observations—is difficult. On the other hand, the 4xCO_2 experiment provides a direct measure of ECS by isolating the climate response to CO_2 forcing alone, with the drawback that it cannot be easily constrained by observations (for reference, Sherwood et al. (2020) provide a 5%–95% likelihood of 2.3–4.7 K).

All WACCM6 configurations exhibit an ECS to a doubling of CO_2 of around 5 K (Figure 11), slightly higher than the CMIP6 multi-model-mean of 3.9 K (Zelinka et al., 2020) and inconsistent with paleoclimate estimates

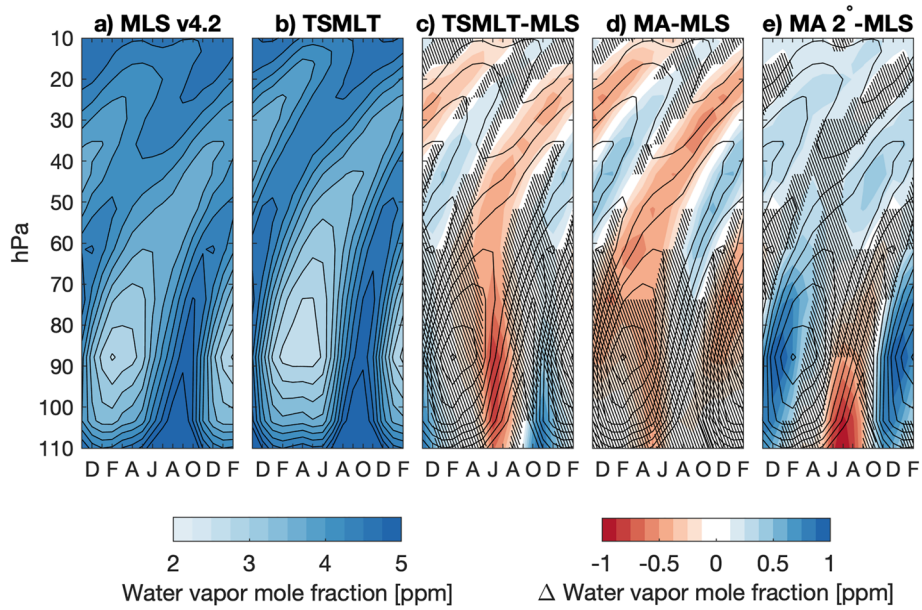

Figure 7. Tropical stratospheric water vapor averaged between 10S and 10N from 2005 to 2014. Shading shows the climatology in (a) and (b) every 0.25 ppm, while shading shows differences in (c)–(e) every 0.125 ppm, with contours indicating the Microwave Limb Sounder (MLS) climatology in (c)–(e). Differences not statistically significantly different from MLS at the 95% confidence level are hatched in (c)–(e), but only where there is shading. All model results are from the historical simulations. Note that in contrast to previous figures, here all comparisons are with observations (to aid in the interpretation of the transport velocity).

19422466, 2023, 9, Downloaded from https://agupubs.onlinelibrary.wiley.com/doi/10.1029/2022MS003579 by Test, Wiley Online Library on [16/10/2023]. See the Terms and Conditions (https://onlinelibrary.wiley.com/terms-and-conditions) on Wiley Online Library for rules of use; OA articles are governed by the applicable Creative Commons License

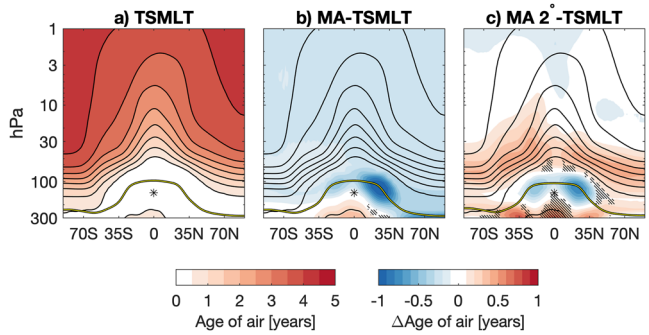

Figure 8. Stratospheric age of air averaged over the historical experiment in (a) troposphere-stratosphere-mesosphere-lower thermosphere (TSMLT) shaded every 0.5 years, and (b–c) the difference in age of air relative to TSMLT shaded every 0.1 years. Hatching indicates differences not statistically significant at the 95% confidence level, but only where there is shading. The tropopause is indicated by the yellow line. The reference location is indicated by the asterisk. All model results are from the historical simulations.

(Zhu et al., 2022). The cloud scheme, and in particular high latitude ice processes, are partially responsible (Gettelman, Hannay, et al., 2019). There is some nonlinearity apparent in the regression, with high top-of-atmosphere radiative flux values well above the regression line in the first few years of the experiment, and a broad cluster at higher global mean surface temperature anomalies and lower top-of-atmosphere radiative fluxes. This behavior is consistent across the different configurations and across other models, though (Andrews et al., 2012).

In summary, we find that climate sensitivity and the simulation of historical climate variability is similar across all WACCM6 configurations and not systematically impacted by either simplified chemistry or coarser resolution.

8. Chemistry and Aerosols

Here we evaluate changes in some key chemical components of the atmosphere between the model versions. In general, we do not expect the MA version to perform that differently than TSMLT in the stratosphere given identical chemistry schemes above the tropopause. Indeed we observe no changes in stratospheric ozone (Figures 12a–12c) except very close to the tropopause; those differences can be traced to the transport of different concentrations of ozone in tropospheric air being advected upward, as the two model configurations do show substantial differences in the troposphere, with up to a 30% difference in the tropical upper troposphere (Figures 12d–12f). Similarities and differences between the two configurations are consistent when considering a period with no increased concentrations of halogens (1850–1900, dotted lines) and a period with higher halogen concentrations (2004–2010, solid lines), as shown in Figures 12g and 12h for the total tropospheric and stratospheric ozone column. The stratospheric ozone column is consistent between all model configurations except over the Antarctic, where the MA 2° configuration shows lower concentrations of around 10 DU in both periods. In the troposphere, the two MA configurations have ozone concentrations ranging between 4 and 2 DU lower than TSMLT at all latitudes during both the low and high halogen concentration time periods. At the pole in the Northern hemisphere the tropospheric ozone column

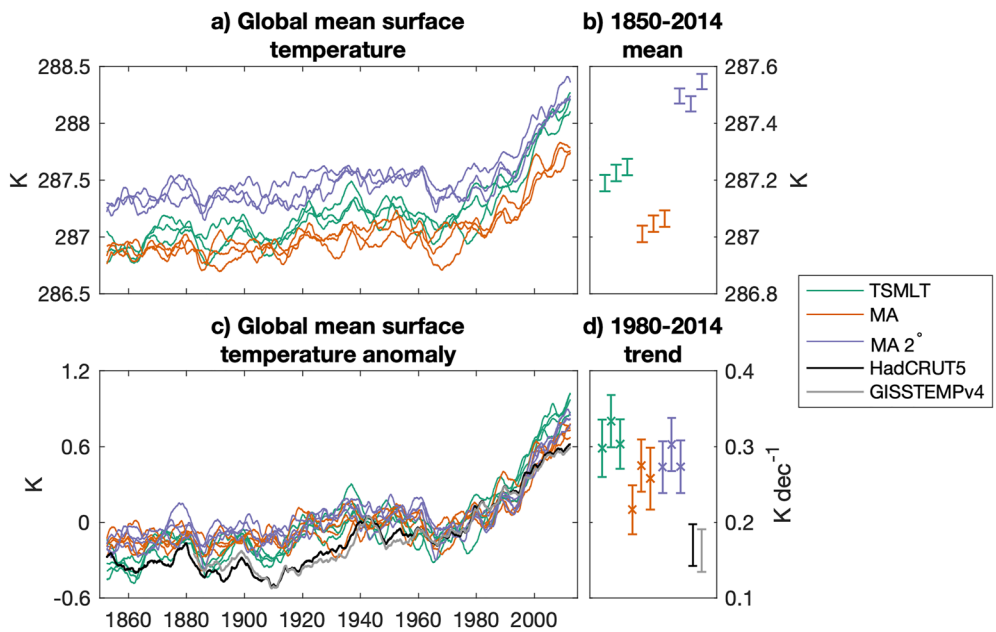

Figure 9. Time series of monthly 5-year running mean (a) absolute global mean surface temperature and (b) global mean surface temperature anomalies, as well as (c) the 1850–2014 average global mean surface temperature and (d) 1980–2014 trend in global mean surface temperature. An x in (d) indicates a trend statistically significantly different from both HadCRUT5 and GISSTEMPv4 at the 95% confidence level.

19422466, 2023, 9, Downloaded from https://agupubs.onlinelibrary.wiley.com/doi/10.1029/2022MS003579 by Test, Wiley Online Library on [16/10/2023]. See the Terms and Conditions (https://onlinelibrary.wiley.com/terms-and-conditions) on Wiley Online Library for rules of use; OA articles are governed by the applicable Creative Commons License

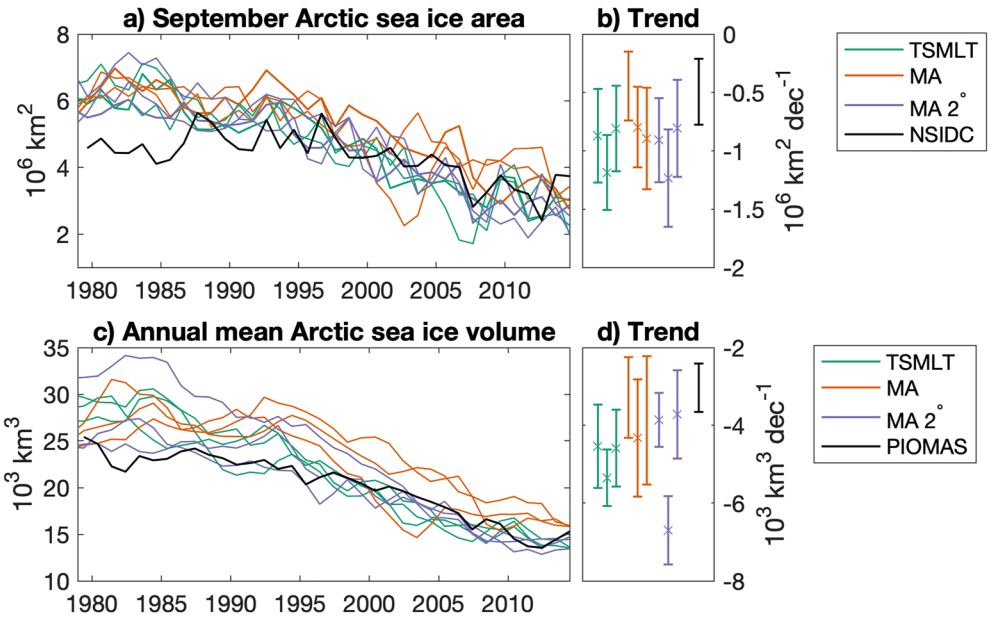

Figure 10. Time series of (a) September Arctic sea ice area and (b) its 1980–2014 trend, and (c) Annual mean Arctic sea ice volume and (d) its 1980–2014 trend. An x in (b) and (d) indicate a trend statistically significantly different from National Snow and Ice Data Center Sea Ice Index (NSIDC) or Pan-Arctic Ice Ocean Modeling and Assimilation System (PIOMAS) at the 95% confidence level.

in the two MA configurations are comparable, but MA 2° shows the lowest column of all configurations at all other latitudes. Some of the largest differences in the tropospheric column are found in the tropics, consistent with the largest changes in tropospheric OH and aerosol species, as we will show later.

In general, the low-ozone bias of the MA 2° configuration is visible throughout the entire evolution of the Antarctic ozone hole (Figure 13a), and is consistent with an older age of air in the polar lower stratosphere (Figure 8c). On the other hand, the two 1° configurations present very similar evolutions up to 2100 under the SSP2-4.5 scenario. Comparisons with Ozone Monitoring Instrument (OMI)/MLS data (Ziemke et al., 2006, 2019) for the ozone column in Figures 12g and 12h for 2004–2010 indicates a very good agreement in the tropics, while at high Southern latitudes all model configurations seem to overestimate stratospheric ozone loss compared to both OMI/MLS and SBUV (Figures 12g and 13a). However, the model configurations better reproduce the evolution

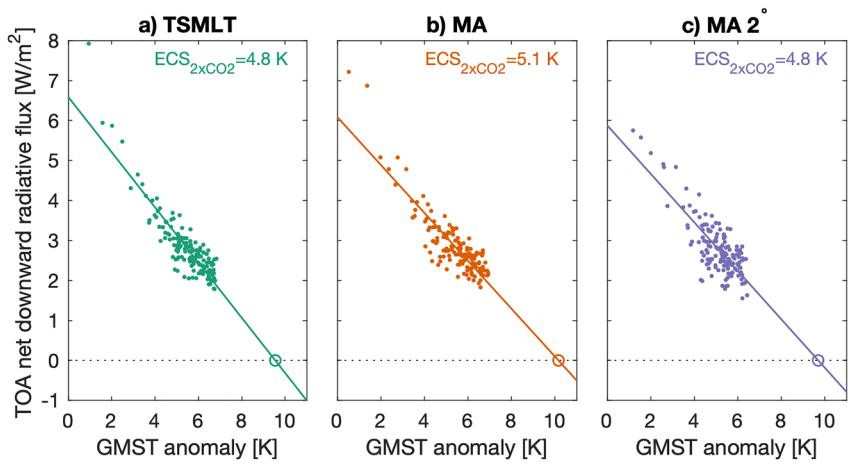

Figure 11. Equilibrium climate sensitivity estimated from the $4xCO_2$ experiment based on the regression between the global mean surface temperature anomaly and the top-of-atmosphere net radiative flux. See text for details.

19422466, 2023, 9, Downloaded from https://agupubs.onlinelibrary.wiley.com/doi/10.1029/2022MS003579 by Test, Wiley Online Library on [16/10/2023]. See the Terms and Conditions (https://onlinelibrary.wiley.com/terms-and-conditions) on Wiley Online Library for rules of use; OA articles are governed by the applicable Creative Commons License

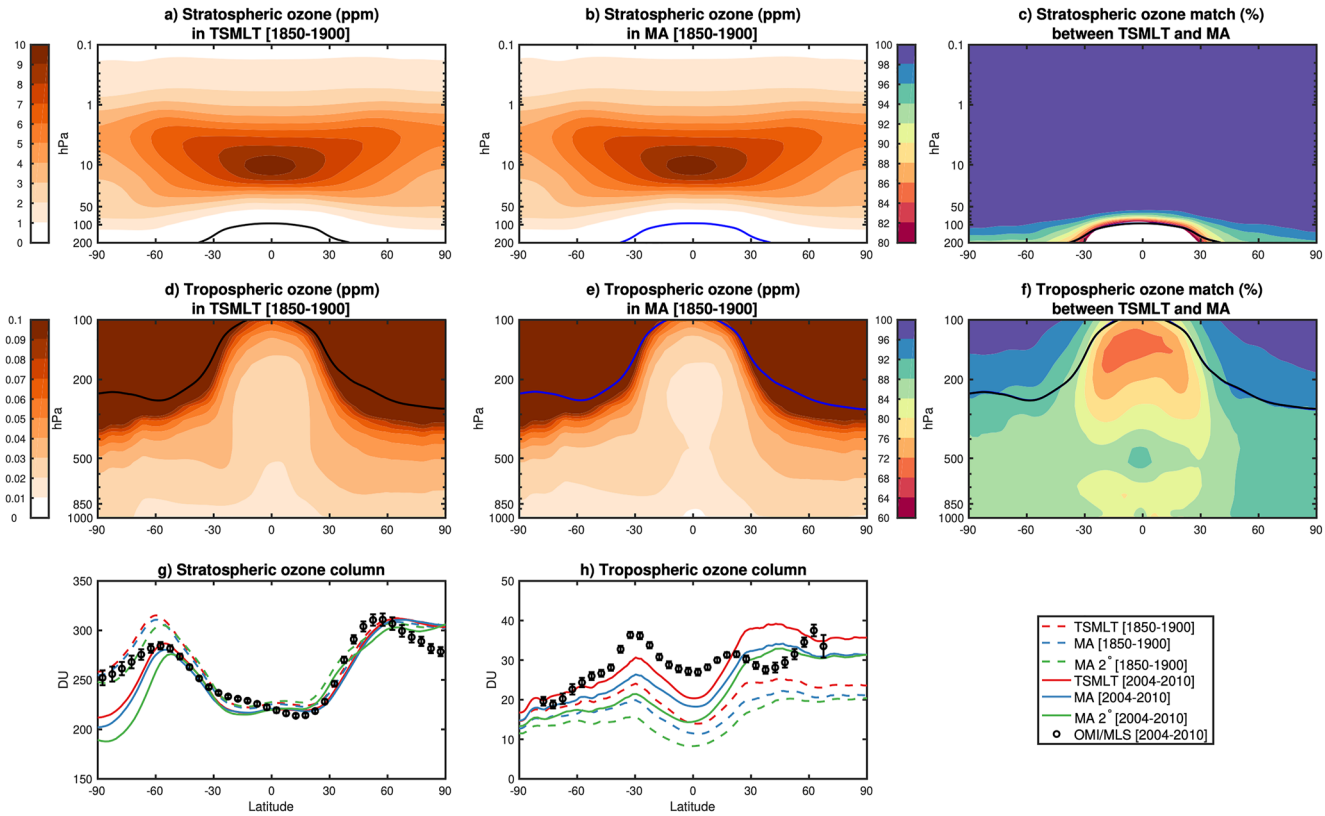

Figure 12. Comparison of atmospheric ozone between troposphere-stratosphere-mesosphere-lower thermosphere (TSMLT) and middle atmosphere (MA) in the period 1850–1900. (a, b) Stratospheric ozone concentration (shaded every 1 ppm). (c) Match (%) between the two Community Earth System Model Version 2 versions for stratospheric ozone, defined as $(100 - |O_{3,TSMLT} - O_{3,MA}|/O_{3,TSMLT})$, shaded every 2%. (d–f) same as the row above, but for tropospheric ozone (note the different color scales, shaded every 0.01 ppm). The tropopause pressure height averaged over the same period is also shown (black for TSMLT, blue for MA). (g, h) Stratospheric and tropospheric ozone column for the two versions and for MA 2°, averaged over 1850–1900 (dashed lines) and over 2004–2010 (continuous lines), and comparison with Ozone Monitoring Instrument (OMI)/Microwave Limb Sounder (MLS) satellite data for the same period (black circles).

of the ozone hole and its peak anomaly relative to the 1970–1989 average (Figure 13b), which aligns the models and observations to the period of peak depletion.

As previous versions of CESM(WACCM) have been used extensively for the assessment of both past volcanic eruptions (Mills et al., 2016) and geoengineering (Tilmes et al., 2021), we also look at differences between the model configurations in terms of stratospheric aerosol optical depth (AOD), which is almost exclusively due to sulfates. The model configurations use the same aerosol microphysical model, MAM4 (Liu et al., 2016), but differences may arise in the concentration and evolution of aerosol precursors. Comparison is provided with the CMIP6 volcanic aerosol data set that is available for the full 1850–2016 period (Eyring et al., 2016), with the 1980–2015 period composed of the Global Space-based Stratospheric Aerosol Climatology (GloSSAC) (Thomason et al., 2018), which combines a large series of ground and space based measurements, and the 1850–1979 period based on a 2-D interactive stratospheric aerosol model (Arfeuille et al., 2014).

Figure 14a shows the global mean stratospheric AOD evolution in the historical period. In all periods with a substantive emission of SO_2 from volcanic eruptions directly in the stratosphere, all model configurations show similar peaks both in magnitude and in timing that coincide with the values found by GloSSAC. However, TSMLT has a consistently lower value of stratospheric AOD than the two MA configurations during periods with no important volcanic activity (prescribed in all models from SO_2 injections following Neely and Schmidt (2016)). This change is also highlighted in Figure 14b, where the differences with TSMLT are shown as a percentage, and the differences drop close to zero in the year following a stratospheric SO_2 injection. This indicates that differences in the baseline stratospheric aerosol load are not due to differences in the underlying stratospheric oxidation process, as also highlighted by the similarities in stratospheric OH shown in Figure 15.

19422466, 2023, 9, Downloaded from https://agupubs.onlinelibrary.wiley.com/doi/10.1029/2022MS003579 by Test, Wiley Online Library on [16/10/2023]. See the Terms and Conditions (https://onlinelibrary.wiley.com/terms-and-conditions) on Wiley Online Library for rules of use; OA articles are governed by the applicable Creative Commons License

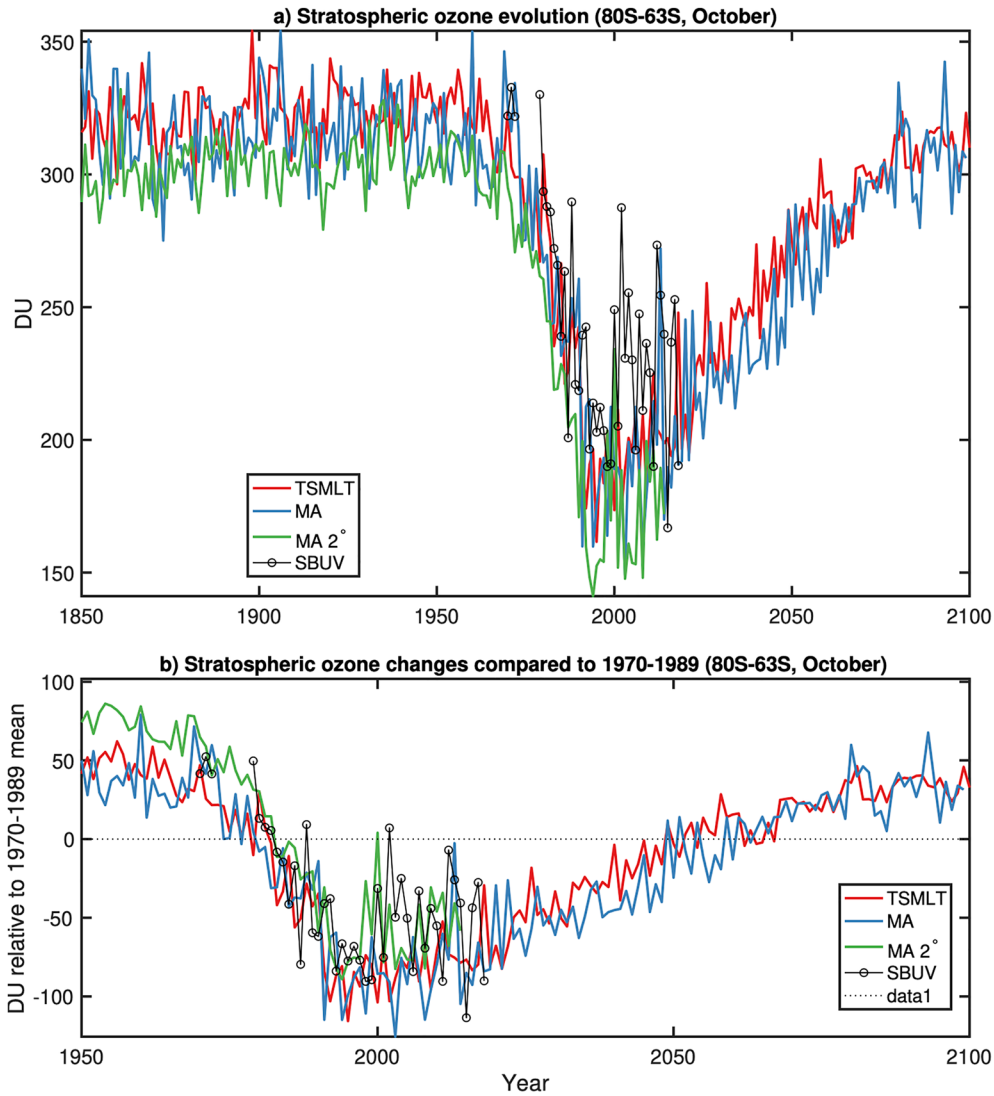

Figure 13. Evolution of Southern Hemispheric Polar Ozone column during October. Solid lines represent the ensemble averages. A comparison with the Solar Backscatter Ultraviolet (SBUV) Merged Ozone Data Set is provided (black line with circles) (McPeters et al., 2013). A 3-year running mean is applied to model results. After 2015, values for the SSP2-4.5 emission scenarios are used. Values are shown for both (a) absolute Dobson units for the period 1850–2100 and (b) Dobson units relative to the 1970–1989 mean for the period 1950–2100.

On the other hand, a comparison of tropospheric OH between the two configurations highlights large differences in MA, where the OH peak in the tropics is located lower down at 300 to 400 hPa. The background stratospheric aerosol layer (also shown in Figure 14c), when unperturbed by the direct injection of SO_2 from volcanic sources, is largely dominated by carbonyl sulphide (COS) (Brühl et al., 2012) and surface SO_2 emissions from minor effusive volcanoes and anthropogenic sources (Neely et al., 2013; Pitari et al., 2016); however, COS is non reactive in the troposphere and only produces SO_x after photolysis above 20 km, and its sources are independent from the model configuration. It is therefore likely that differences in the stratospheric AOD are mainly driven by differences in upper tropospheric SO_2 oxidation and subsequent transport of newly formed aerosols into the lowermost stratosphere. This is further confirmed by looking at the different aerosol modes for sulfate (Figure S2 in Supporting Information S1). In quiescent periods, the main difference in the aerosol burden is found in the Aitken (smaller) mode in the upper troposphere and lower stratosphere, while in the Accumulation (intermediate) and Coarse (larger) mode, the two configurations are highly comparable. The MA configurations are show better agreement with the CMIP6 volcanic aerosol data set, which in the pre-1980 period is based solely on interactive stratospheric aerosol simulations and may thus miss the correct tropospheric contribution present in TSMLT.

19422466, 2023, 9, Downloaded from https://agupubs.onlinelibrary.wiley.com/doi/10.1029/2022MS003579 by Test, Wiley Online Library on [16/10/2023]. See the Terms and Conditions (https://onlinelibrary.wiley.com/terms-and-conditions) on Wiley Online Library for rules of use; OA articles are governed by the applicable Creative Commons License

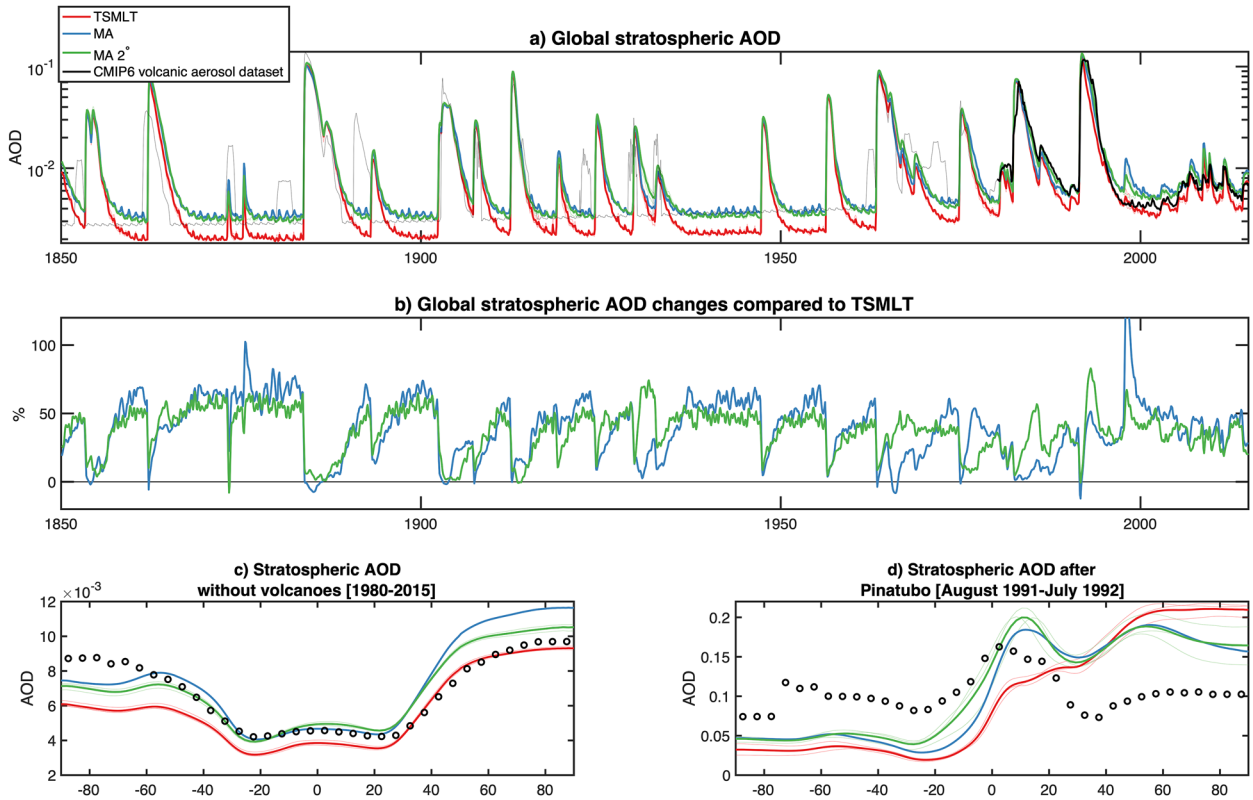

Figure 14. (a) Monthly means of globally-averaged stratospheric aerosol optical depth (AOD) in the historical period for troposphere-stratosphere-mesosphere-lower thermosphere (TSMLT) (red), middle atmosphere (MA) (blue), MA 2° (green) and the Coupled Model Intercomparison Project Phase 6 (CMIP6) volcanic aerosol data set (Eyring et al., 2016); the Global Space-based Stratospheric Aerosol Climatology period (Thomason et al., 2018) (1980–2015) has been marked with a thicker line. (b) Percent difference between TSMLT and MA, and TSMLT and MA 2° smoothed with a 3-month running mean. (c) Latitudinal mean of stratospheric AOD in periods with no volcanic activity (chosen as all months in panel (a) where global stratospheric AOD does not go above 0.001) between 1980 and 2015. (d) As in (c), but averaged over the 18 months after the Pinatubo June 1991 eruption. Black dots are from the same CMIP6 data sets as panel (a).

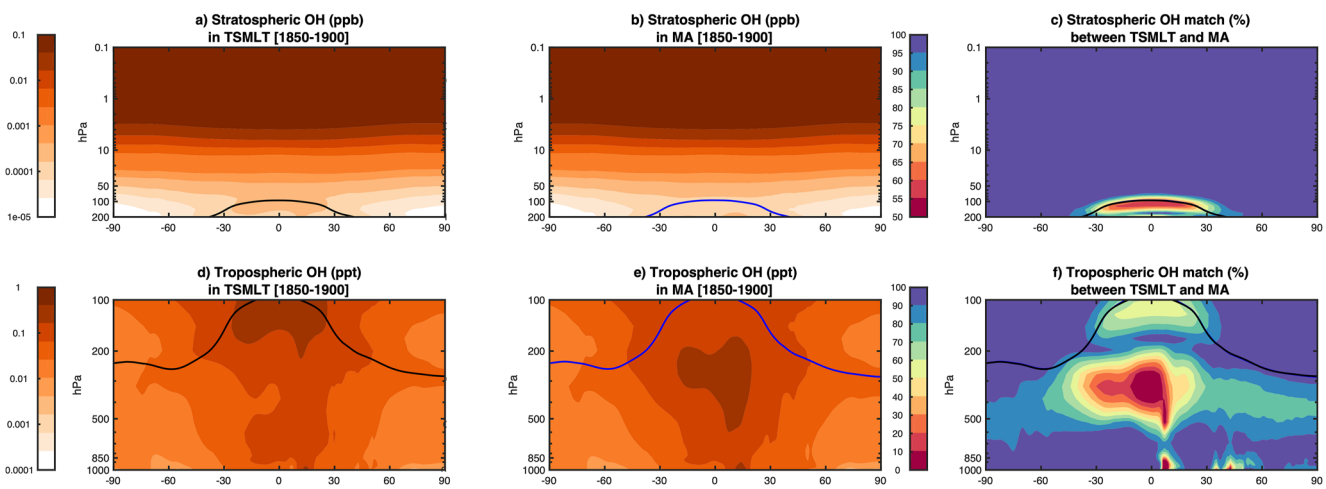

Figure 15. Comparison of atmospheric OH radical between troposphere-stratosphere-mesosphere-lower thermosphere (TSMLT) and middle atmosphere (MA) in the historical period. (a, b) Stratospheric OH concentration (ppm, log-scale) between 1850 and 1900. (c) Match between the two Community Earth System Model Version 2 versions for stratospheric OH defined as $((100 - |OH_{TSMLT} - OH_{MA}|)/OH_{TSMLT})$, shaded every 5%. (d–f) Same as the row above, but for tropospheric OH (note the difference color scales). The tropopause pressure height averaged over the same period is also shown (black for TSMLT, blue for MA).

19422466, 2023, 9, Downloaded from https://agupubs.onlinelibrary.wiley.com/doi/10.1029/2022MS003579 by Test, Wiley Online Library on [16/10/2023]. See the Terms and Conditions (https://onlinelibrary.wiley.com/terms-and-conditions) on Wiley Online Library for rules of use; OA articles are governed by the applicable Creative Commons License

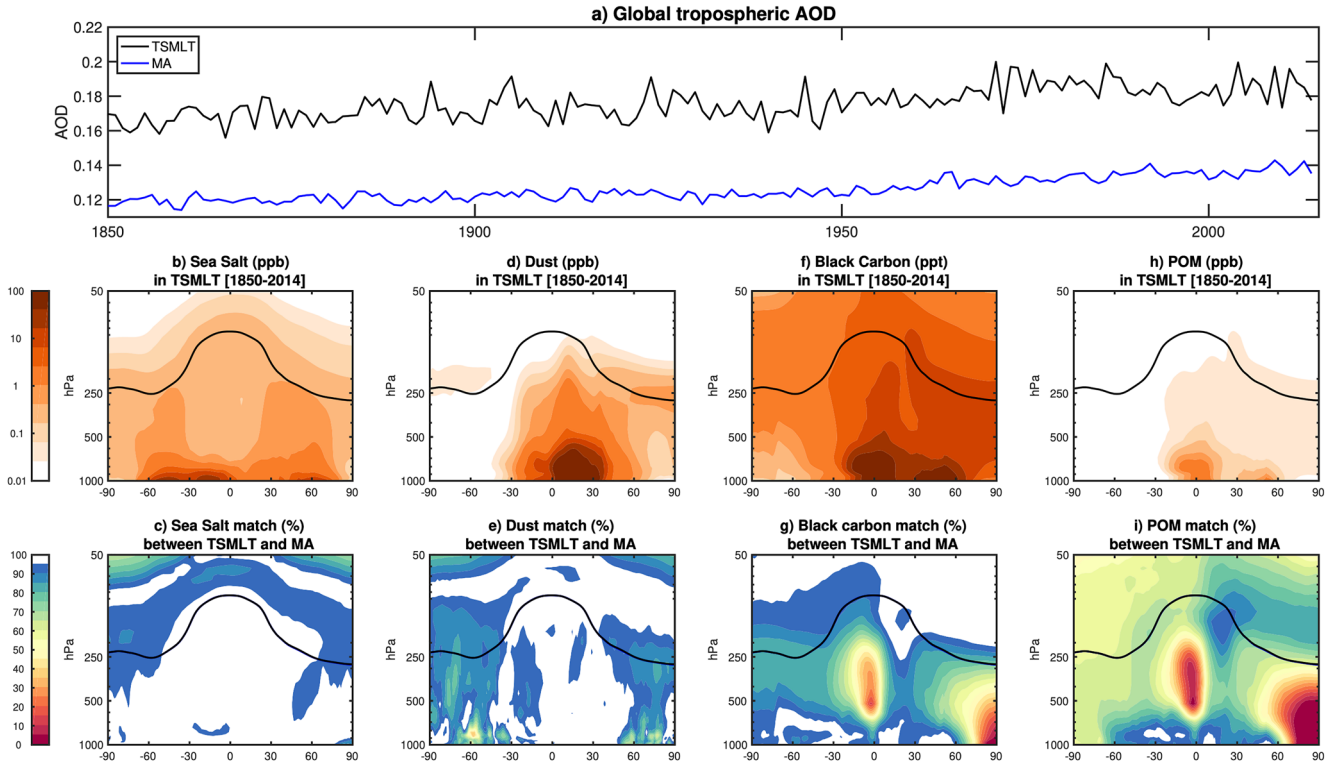

Figure 16. (a) Annual means of globally-averaged tropospheric aerosol optical depth (AOD) in the historical period for troposphere-stratosphere-mesosphere-lower thermosphere (TSMLT) (black) and middle atmosphere (MA) (blue). (b) Sea salt concentration (ppb) in TSMLT. (c) match between TSMLT and MA defined as $((100 - |\chi_{TSMLT} - \chi_{MA}|)/\chi_{TSMLT})$. (d–e, f–g, h–i) Same as (b–c), for dust, Black carbon and primary organic matter (POM).

Figure 14d also shows the latitudinal distribution of aerosols in the post-Pinatubo months: while the overall increase in AOD is correctly captured, there are differences in the hemispheric transport of the aerosols, as also highlighted in Quaglia et al. (2023) for other models with interactive aerosol treatments. This is caused in part by how the initial SO_2 plume is prescribed, but also by the specific meteorological conditions at the time of the real eruption, which are not properly captured by free-running simulations like the ones under analyses.

The analyses of other, mostly tropospheric, aerosol species (Figure 16) also indicate that the lack of a proper representation of oxidants due to a very simplified chemical description in the troposphere tends to not affect larger particles such as those formed by sea salt and dust, whereas black carbon and primary organic matter (POM), which are emitted in a separated, smaller primary carbon mode (Liu et al., 2016) and then aged into larger modes, are much lower due to the lack of aging processes into SOA as present in the TMSLT configuration (Tilmes et al., 2019), which results in reduced aging of BC and POM, and therefore a slower removal. Overall, given that in MAM4 different aerosol species are treated as internally mixed for number concentration purposes (i.e., all aerosol species are described by a shared number concentration, but have different masses), this would then tend to produce similar changes in black carbon as well in the primary nucleation and Atkinson mode. Previous work has also shown how this internal mixing assumption can create unnatural behavior in ice clouds in response to sulfate aerosol forcings (Visioni et al., 2022). Differences in surface dust as observed in Figure 16 may on the other hand be due to slight differences in the surface climate (Figure 9), resulting in different regional emissions.

9. Conclusions

We evaluated two simplified chemistry configurations of CESM2(WACCM6) at nominal 1 and 2° horizontal resolution against observations, a reanalysis, and a scientifically-validated configuration with comprehensive TSMLT chemistry. A summary of all results can be seen in Table 3. Simplifying the chemistry—by eliminating halogen precursors, organic chemistry, and secondary organic aerosol formation—has little impact on

19422466, 2023, 9, Downloaded from https://agupubs.onlinelibrary.wiley.com/doi/10.1029/2022MS003579 by Test, Wiley Online Library on [16/10/2023]. See the Terms and Conditions (https://onlinelibrary.wiley.com/terms-and-conditions) on Wiley Online Library for rules of use; OA articles are governed by the applicable Creative Commons License

Table 3
Summary Table of Metrics, Fields, and Processes Examined in This Study, Whether They Are More Impacted by Variations in Horizontal Resolution or Chemistry Scheme Complexity, and the Relevant Figures/Tables for the Analysis

Metric, field, or process	More impacted by horizontal resolution or chemistry	Relevant figures
Zonal mean temperature	Horizontal resolution	Figure 1
Zonal mean zonal wind	Horizontal resolution	Figure 2
Polar vortex variability	Neither	Figures 3 and 4
Tropical stratospheric upwelling	Horizontal resolution	Figure 6
Water vapor tape recorder	Horizontal resolution	Figure 7
Age of air	Both	Figure 8
Cloud radiative effects	Horizontal resolution	Table 2
Surface temperature and trend	Both	Table 2, Figure 9
Arctic sea ice area/volume	Neither	Figure 10
Climate sensitivity	Neither	Figure 11
Stratospheric ozone	Horizontal resolution	Figures 12 and 13
Tropospheric ozone	Both	Figure 12
Stratospheric AOD	Both	Figure 14

Note. For the second column, "both" means that varying either horizontal resolution or chemical complexity is impactful, while "neither" means neither varying horizontal resolution nor chemical complexity is impactful.

zonal mean climate, middle atmosphere variability, or climate sensitivity. It does reduce the absolute global mean surface temperature (of the nominal 1° horizontal configuration), which may be due to an elevated background stratospheric AOD.

While there are some differences in stratospheric ozone incurred by simplifying the chemistry scheme, they are generally smaller than the impact of coarsening the nominal horizontal resolution from 1 to 2°. Again, this may be due to differences in the parameterized gravity wave drag, which can be addressed with more targeted tuning in future releases. As long as model users do not require a faithful recreation of tropospheric chemistry and background aerosols in the upper troposphere/lower stratosphere, CESM2(WACCM6) with middle atmosphere chemistry can probably be used in lieu of CESM2(WACCM6) with comprehensive chemistry.

Coarsening the nominal horizontal resolution from 1 to 2° has little material impact on zonal mean climate, middle atmospheric variability, or climate sensitivity, though the circulation of the mesosphere and lower thermosphere and middle atmospheric transport show some significant changes. Where satellite observations of the upper atmosphere have adequate coverage, MA 2° tends to have smaller biases. The 2° simplified chemistry configuration—without an internally-generated QBO—may be appropriate for applications where a specified QBO is acceptable.

These two configurations of CESM2(WACCM6)—nominal 1 and 2° horizontal resolution with middle atmosphere chemistry—are 35% and 86% computationally cheaper than the nominal 1° horizontal configuration of CESM2(WACCM6) with comprehensive chemistry. In some cases, they may provide support for ensemble experiments and long climate integrations to study climate change, geoengineering, and historical variability. Users will need to keep in mind the limitations of these configurations, but can be confident there are no major caveats to their zonal mean climate or their global mean response to forcings. Future versions of CESM(WACCM) will continue to support economical configurations to ensure the user community has the ability to simulate the coupling of the whole atmosphere to the Sun and Earth systems.

Data Availability Statement

MERRA2 (Global Modeling and Assimilation Office, 2015) can be accessed from the NASA Goddard Earth Sciences (GES) Distributed Active Archive Center (DAAC) at https://disc.gsfc.nasa.gov/datasets?project=MERRA-2. SABER (GATS, Inc, 2015) retrievals are accessible from GATS, Inc. at http://saber.gats-inc.com/data.php, while MLS v4.2 retrievals (Lambert et al., 2015) are accessible from the NASA Jet Propulsion Laboratory at https://mls.jpl.nasa.gov/. The merged SBUV ozone retrievals (Goddard Space Flight Center, 2022) can be downloaded directly from https://acd-ext.gsfc.nasa.gov/Data_services/merged/index.html. GISSTEMPv4 (GISTEMP Team, 2022) is available from the NASA Goddard Institute for Space Studies at https://data.giss.nasa.gov/gistemp/, while CRUTEM5 (Climatic Research Unit (University of East Anglia) and Met Office, 2022) is available from the Met Office Hadley Center at https://www.metoffice.gov.uk/hadobs/crutem5/. The NSIDC Sea Ice Index, Version 3 (Fetterer et al., 2017), is available via FTP from https://nsidc.org/data/g02135/versions/3, and PIOMAS sea ice volume (Schweiger et al., 2011) is available at http://psc.apl.uw.edu/wordpress/wp-content/uploads/schweiger/ice_volume/PIOMAS.2sst.monthly.Current.v2.1.txt. All WACCM6 output is available on the Earth System Grid, accessed through the CMIP6 portal at https://esgf-node.llnl.gov/search/cmip6/.

19422466, 2023, 9, Downloaded from https://agupubs.onlinelibrary.wiley.com/doi/10.1029/2022MS003579 by Test, Wiley Online Library on [16/10/2023]. See the Terms and Conditions (https://onlinelibrary.wiley.com/terms-and-conditions) on Wiley Online Library for rules of use; OA articles are governed by the applicable Creative Commons License

Acknowledgments
The CESM project is supported primarily by the National Science Foundation (NSF). This work was supported by the National Center for Atmospheric Research, which is a major facility sponsored by the National Science Foundation under Cooperative Agreement 1852977. Computing and data storage resources, including the Cheyenne supercomputer (doi: 10.5065/D6RX99HX), were provided by the Computational and Information Systems Laboratory (CISL) at NCAR. Portions of this study were supported by the Regional and Global Model Analysis (RGMA) component of the Earth and Environmental System Modeling Program of the U.S. Department of Energy's Office of Biological & Environmental Research (BER) via National Science Foundation IA 1844590. The authors thank three reviewers for their constructive comments and suggestions.

References

Abalos, M., Calvo, N., Benito-Barca, S., Garny, H., Hardiman, S. C., Lin, P., et al. (2021). The Brewer-Dobson circulation in CMIP6. *Atmospheric Chemistry and Physics*, *21*(17), 13571–13591. https://doi.org/10.5194/acp-21-13571-2021

Abalos, M., Polvani, L., Calvo, N., Kinnison, D., Ploeger, F., Randel, W., & Solomon, S. (2019). New insights on the impact of ozone-depleting substances on the Brewer-Dobson circulation. *Journal of Geophysical Research: Atmospheres*, *124*(5), 2435–2451. https://doi.org/10.1029/2018JD029301

Andersson, M. E., Verronen, P. T., Marsh, D. R., Päivärinta, S.-M., & Plane, J. M. C. (2016). WACCM-D: Improved modeling of nitric acid and active chlorine during energetic particle precipitation. *Journal of Geophysical Research: Atmospheres*, *121*(17), 10328–10341. https://doi.org/10.1002/2015JD024173

Andrews, T., Gregory, J. M., Webb, M. J., & Taylor, K. E. (2012). Forcing, feedbacks and climate sensitivity in CMIP5 coupled atmosphere-ocean climate models. *Geophysical Research Letters*, *39*(9), L09712. https://doi.org/10.1029/2012GL051607

Arfeuille, F., Weisenstein, D., Mack, H., Rozanov, E., Peter, T., & Brönnimann, S. (2014). Volcanic forcing for climate modeling: A new microphysics-based data set covering years 1600–present. *Climate of the Past*, *10*(1), 359–375. https://doi.org/10.5194/cp-10-359-2014

Aubry, T. J., Staunton-Sykes, J., Marshall, L. R., Haywood, J., Abraham, N. L., & Schmidt, A. (2021). Climate change modulates the stratospheric volcanic sulfate aerosol lifecycle and radiative forcing from tropical eruptions. *Nature Communications*, *12*(1), 4708. https://doi.org/10.1038/s41467-021-24943-7

Baldwin, M. P., Ayarzagüena, B., Birner, T., Butchart, N., Butler, A. H., Charlton-Perez, A. J., et al. (2021). Sudden stratospheric warmings. *Reviews of Geophysics*, *59*(1), e2020RG000708. https://doi.org/10.1029/2020RG000708

Baldwin, M. P., Gray, L. J., Dunkerton, T. J., Hamilton, K., Haynes, P. H., Randel, W. J., et al. (2001). The quasi-biennial oscillation. *Reviews of Geophysics*, *39*(2), 179–229. https://doi.org/10.1029/1999RG000073

Beljaars, A. C. M., Brown, A. R., & Wood, N. (2004). A new parametrization of turbulent orographic form drag. *Quarterly Journal of the Royal Meteorological Society*, *130*(599), 1327–1347. https://doi.org/10.1256/qj.03.73

Brühl, C., Lelieveld, J., Crutzen, P. J., & Tost, H. (2012). The role of carbonyl sulphide as a source of stratospheric sulphate aerosol and its impact on climate. *Atmospheric Chemistry and Physics*, *12*(3), 1239–1253. https://doi.org/10.5194/acp-12-1239-2012

Butchart, N., & Scaife, A. (2001). Removal of chlorofluorocarbons by increased mass exchange between the stratosphere and troposphere in a changing climate. *Nature*, *410*(6830), 799–802. https://doi.org/10.1038/35071047

Chabrillat, S., Kockarts, G., Fonteyn, D., & Brasseur, G. (2002). Impact of molecular diffusion on the CO_2 distribution and the temperature in the mesosphere. *Geophysical Research Letters*, *29*(15), 19-1–19-4. https://doi.org/10.1029/2002GL015309

Charlton, A. J., & Polvani, L. M. (2007). A new look at stratospheric sudden warmings. Part I: Climatology and modeling benchmarks. *Journal of Climate*, *20*(3), 449–469. https://doi.org/10.1175/JCLI3996.1

Chrysanthou, A., Maycock, A. C., & Chipperfield, M. P. (2020). Decomposing the response of the stratospheric Brewer-Dobson circulation to an abrupt quadrupling in CO_2. *Weather and Climate Dynamics*, *1*(1), 155–174. https://doi.org/10.5194/wcd-1-155-2020

Climatic Research Unit (University of East Anglia) and Met Office. (2022). HadCRUT5 analysis [Dataset]. Retrieved from https://crudata.uea.ac.uk/cru/data/temperature/#sciref

Damiani, A., Funke, B., López Puertas, M., Santee, M. L., Cordero, R. R., & Watanabe, S. (2016). Energetic particle precipitation: A major driver of the ozone budget in the Antarctic upper stratosphere. *Geophysical Research Letters*, *43*(7), 3554–3562. https://doi.org/10.1002/2016GL068279

Danabasoglu, G., Bates, S. C., Briegleb, B. P., Jayne, S. R., Jochum, M., Large, W. G., et al. (2012). The CCSM4 ocean component. *Journal of Climate*, *25*(5), 1361–1389. https://doi.org/10.1175/JCLI-D-11-00091.1

Danabasoglu, G., Lamarque, J.-F., Bacmeister, J., Bailey, D. A., DuVivier, A. K., Edwards, J., et al. (2020). The Community Earth System Model Version 2 (CESM2). *Journal of Advances in Modeling Earth Systems*, *12*(2), e2019MS001916. https://doi.org/10.1029/2019MS001916

Dawkins, E. C. M., Feofilov, A., Rezac, L., Kutepov, A. A., Janches, D., Höffner, J., et al. (2018). Validation of SABER v2.0 operational temperature data with ground-based lidars in the mesosphere-lower thermosphere region (75-105 km). *Journal of Geophysical Research: Atmospheres*, *123*(17), 9916–9934. https://doi.org/10.1029/2018JD028742

Dunkerton, T. J., & Delisi, D. P. (1985). Climatology of the equatorial lower stratosphere. *Journal of the Atmospheric Sciences*, *42*(4), 376–396. https://doi.org/10.1175/1520-0469(1985)042⟨0376:COTELS⟩2.0.CO;2

Emmons, L. K., Schwantes, R. H., Orlando, J. J., Tyndall, G., Kinnison, D., Lamarque, J.-F., et al. (2020). The chemistry mechanism in the Community Earth System Model Version 2 (CESM2). *Journal of Advances in Modeling Earth Systems*, *12*(4), e2019MS001882. https://doi.org/10.1029/2019MS001882

Eyring, V., Bony, S., Meehl, G. A., Senior, C. A., Stevens, B., Stouffer, R. J., & Taylor, K. E. (2016). Overview of the Coupled Model Intercomparison Project Phase 6 (CMIP6) experimental design and organization. *Geoscientific Model Development*, *9*(5), 1937–1958. https://doi.org/10.5194/gmd-9-1937-2016

Fang, X., Pyle, J. A., Chipperfield, M. P., Daniel, J. S., Park, S., & Prinn, R. G. (2019). Challenges for the recovery of the ozone layer. *Nature Geoscience*, *12*(8), 592–596. https://doi.org/10.1038/s41561-019-0422-7

Fetterer, F., Knowles, K., Meier, W. N., Savoie, M., & Windnagel, A. K. (2017). Sea ice index Version 3 [Dataset]. https://doi.org/10.7265/N5K072F8

Frith, S. M., Kramarova, N. A., Stolarski, R. S., McPeters, R. D., Bhartiaand, P. K., & Labow, G. J. (2014). Recent changes in total column ozone based on the SBUV version 8.6 merged ozone data set. *Journal of Geophysical Research: Atmospheres*, *119*(16), 9735–9751. https://doi.org/10.1002/2014JD021889

Fujiwara, M., Wright, J. S., Manney, G. L., Gray, L. J., Anstey, J., Birner, T., et al. (2017). Introduction to the SPARC Reanalysis Intercomparison Project (S-RIP) and overview of the reanalysis systems. *Atmospheric Chemistry and Physics*, *17*(2), 1417–1452. https://doi.org/10.5194/acp-17-1417-2017

Garcia, R. R., López-Puertas, M., Funke, B., Marsh, D. R., Kinnison, D. E., Smith, A. K., & González-Galindo, F. (2014). On the distribution of CO_2 and CO in the mesosphere and lower thermosphere. *Journal of Geophysical Research: Atmospheres*, *119*(9), 5700–5718. https://doi.org/10.1002/2013JD021208

Garcia, R. R., Marsh, D. R., Kinnison, D. E., Boville, B. A., & Sassi, F. (2007). Simulation of secular trends in the middle atmosphere, 1950-2003. *Journal of Geophysical Research*, *112*(D9), D09301. https://doi.org/10.1029/2006JD007485

Garcia, R. R., Randel, W. J., & Kinnison, D. E. (2011). On the determination of age of air trends from atmospheric trace species. *Journal of the Atmospheric Sciences*, *68*(1), 139–154. https://doi.org/10.1175/2010JAS3527.1

Garcia, R. R., & Richter, J. H. (2019). On the momentum budget of the quasi-biennial oscillation in the whole atmosphere community climate model. *Journal of the Atmospheric Sciences*, *76*(1), 69–87. https://doi.org/10.1175/JAS-D-18-0088.1

19422466, 2023, 9, Downloaded from https://agupubs.onlinelibrary.wiley.com/doi/10.1029/2022MS003579 by Test, Wiley Online Library on [16/10/2023]. See the Terms and Conditions (https://onlinelibrary.wiley.com/terms-and-conditions) on Wiley Online Library for rules of use; OA articles are governed by the applicable Creative Commons License

Garcia, R. R., Smith, A. K., Kinnison, D. E., de la Cámara, Á., & Murphy, D. J. (2017). Modification of the gravity wave parameterization in the Whole Atmosphere Community Climate Model: Motivation and results. *Journal of the Atmospheric Sciences*, *74*(1), 275–291. https://doi.org/10.1175/JAS-D-16-0104.1

Garcia, R. R., & Solomon, S. (1985). The effect of breaking gravity waves on the dynamics and chemical composition of the mesosphere and lower thermosphere. *Journal of Geophysical Research*, *90*(D2), 3850–3868. https://doi.org/10.1029/JD090iD02p03850

GATS, Inc. (2015). Sounding of the atmosphere using broadband emission radiometry v2.0 [Dataset]. Retrieved from https://data.gats-inc.com/saber/custom/Temp_O3/v2.0/

Gelaro, R., McCarty, W., Suàrez, M. J., Todling, R., Molod, A., Takacs, L., et al. (2017). The Modern-Era Retrospective Analysis for Research and Applications, Version 2 (MERRA-2). *Journal of Climate*, *30*(14), 5419–5454. https://doi.org/10.1175/JCLI-D-16-0758.1

Gettelman, A., Hannay, C., Bacmeister, J. T., Neale, R. B., Pendergrass, A. G., Danabasoglu, G., et al. (2019). High climate sensitivity in the Community Earth System Model Version 2 (CESM2). *Geophysical Research Letters*, *46*(14), 8329–8337. https://doi.org/10.1029/2019GL083978

Gettelman, A., Mills, M. J., Kinnison, D. E., Garcia, R. R., Smith, A. K., Marsh, D. R., et al. (2019). The Whole Atmosphere Community Climate Model Version 6 (WACCM6). *Journal of Geophysical Research: Atmospheres*, *124*(23), 12380–12403. https://doi.org/10.1029/2019JD030943

Gettelman, A., & Morrison, H. (2015). Advanced two-moment bulk microphysics for global models. Part I: Off-line tests and comparison with other schemes. *Journal of Climate*, *28*(3), 1268–1287. https://doi.org/10.1175/JCLI-D-14-00102.1

GISTEMP Team. (2022). GISS Surface Temperature Analysis (GISTEMP) Version 4 [Dataset]. NASA Goddard Institute for Space Studies. Retrieved from https://data.giss.nasa.gov/gistemp/

Glanville, A. A., & Birner, T. (2017). Role of vertical and horizontal mixing in the tape recorder signal near the tropical tropopause. *Atmospheric Chemistry and Physics*, *17*(6), 4337–4353. https://doi.org/10.5194/acp-17-4337-2017

Global Modeling and Assimilation Office. (2015). inst3_3d_asm_Np: MERRA-2 3D IAU State, meteorology instantaneous 3-hourly (p-coord, 0.625x0.5L42) Version 5.12.4 [Dataset]. Goddard Space Flight Center Distributed Active Archive Center (GSFC DAAC). https://doi.org/10.5067/2E096JV59PK7

Goddard Space Flight Center. (2022). SBUV (Version 8.7) merged total and profile ozone data sets [Dataset]. Retrieved from https://acd-ext.gsfc.nasa.gov/Data_services/merged/index.html

Golaz, J.-C., Larson, V. E., & Cotton, W. R. (2002). A PDF-based model for boundary layer clouds. Part I: Method and model description. *Journal of the Atmospheric Sciences*, *59*(24), 3540–3551. https://doi.org/10.1175/1520-0469(2002)059⟨3540:APBMFB⟩2.0.CO;2

Gregory, J. M., Ingram, W. J., Palmer, M. A., Jones, G. S., Stott, P. A., Thorpe, R. B., & Williams, K. D. (2004). A new method for diagnosing radiative forcing and climate sensitivity. *Geophysical Research Letters*, *31*(3), L03205. https://doi.org/10.1029/2003GL018747

Guenther, A. B., Jiang, X., Heald, C. L., Sakulyanontvittaya, T., Duhl, T., Emmons, L. K., & Wang, X. (2012). The Model of Emissions of Gases and Aerosols from Nature Version 2.1 (MEGAN2.1): An extended and updated framework for modeling biogenic emissions. *Geoscientific Model Development*, *5*(6), 1471–1492. https://doi.org/10.5194/gmd-5-1471-2012

Hodzic, A., Kasibhatla, P. S., Jo, D. S., Cappa, C. D., Jimenez, J. L., Madronich, S., & Park, R. J. (2016). Rethinking the global secondary organic aerosol (SOA) budget: Stronger production, faster removal, shorter lifetime. *Atmospheric Chemistry and Physics*, *16*(12), 7917–7941. https://doi.org/10.5194/acp-16-7917-2016

Hoesly, R., Smith, S., Feng, L., Klimont, Z., Janssens-Maenhout, G., Pitkanen, T., et al. (2017). *Historical emissions (1750 - 2014) - CEDS - v2017-05-18*. Earth System Grid Federation. https://doi.org/10.22033/ESGF/input4MIPs.1241

Hoesly, R., Smith, S. J., Feng, L., Klimont, Z., Janssens-Maenhout, G., Pitkanen, T., et al. (2018). Historical (1750–2014) anthropogenic emissions of reactive gases and aerosols from the Community Emissions Data System (CEDS). *Geoscientific Model Development*, *11*(1), 369–408. https://doi.org/10.5194/gmd-11-369-2018

Holt, L. A., Lott, F., Garcia, R. R., Kiladis, G. N., Cheng, Y.-M., Anstey, J. A., et al. (2022). An evaluation of tropical waves and wave forcing of the QBO in the QBOi models. *Quarterly Journal of the Royal Meteorological Society*, *148*(744), 1541–1567. https://doi.org/10.1002/qj.3827

Hunke, E. C., Lipscomb, W. H., Turner, A. K., Jeffery, N., & Elliott, S. (2015). *CICE: The Los Alamos Sea Ice Model. Documentation and software user's manual*. Version 5.1 (Tech. Rep. LA-CC-06-012: T-3 Fluid Dynamics Group). Los Alamos National Laboratory.

Iacono, M. J., Delamere, J. S., Mlawer, E. J., Shephard, M. W., Clough, S. A., & Collins, W. D. (2008). Radiative forcing by long-lived greenhouse gases: Calculations with the AER radiative transfer models. *Journal of Geophysical Research*, *113*(D13), D13103. https://doi.org/10.1029/2008JD009944

Kinnison, D. E., Brasseur, G. P., Walters, S., Garcia, R. R., Marsh, D. R., Sassi, F., et al. (2007). Sensitivity of chemical tracers to meteorological parameters in the MOZART-3 chemical transport model. *Journal of Geophysical Research*, *112*(D20), D20302. https://doi.org/10.1029/2006JD007879

Kravitz, B., Robock, A., Tilmes, S., Boucher, O., English, J. M., Irvine, P. J., et al. (2015). The Geoengineering Model Intercomparison Project Phase 6 (GeoMIP6): Simulation design and preliminary results. *Geoscientific Model Development*, *8*(10), 3379–3392. https://doi.org/10.5194/gmd-8-3379-2015

Lambert, A., Read, W., & Livesey, N. (2015). MLS/Aura level 2 water vapor (H_2O) mixing ratio V004 [Dataset]. Goddard Earth Sciences Data and Information Services Center (GES DISC). https://doi.org/10.5067/Aura/MLS/DATA2009

Lambert, A., Read, W. G., Livesey, N. J., Santee, M. L., Manney, G. L., Froidevaux, L., et al. (2007). Validation of the Aura Microwave Limb Sounder middle atmosphere water vapor and nitrous oxide measurements. *Journal of Geophysical Research*, *112*(D24), D24S36. https://doi.org/10.1029/2007JD008724

Larson, V. E. (2017). CLUBB-SILHS: A parameterization of subgrid variability in the atmosphere. arXiv preprint arXiv:1711.03675.

Lawrence, D. M., Fisher, R. A., Koven, C. D., Oleson, K. W., Swenson, S. C., Bonan, G., et al. (2019). The Community Land Model Version 5: Description of new features, benchmarking, and impact of forcing uncertainty. *Journal of Advances in Modeling Earth Systems*, *11*(12), 4245–4287. https://doi.org/10.1029/2018MS001583

Lenssen, N. J. L., Schmidt, G. A., Hansen, J. E., Menne, M. J., Persin, A., Ruedy, R., & Zyss, D. (2019). Improvements in the GISTEMP uncertainty model. *Journal of Geophysical Research: Atmospheres*, *124*(12), 6307–6326. https://doi.org/10.1029/2018JD029522

Li, H., Wigmosta, M. S., Wu, H., Huang, M., Ke, Y., Coleman, A. M., & Leung, L. R. (2013). A physically based runoff routing model for land surface and earth system models. *Journal of Hydrometeorology*, *14*(3), 808–828. https://doi.org/10.1175/JHM-D-12-015.1

Lin, S.-J., & Rood, R. B. (1997). An explicit flux-form semi-Lagrangian shallow-water model on the sphere. *Quarterly Journal of the Royal Meteorological Society*, *123*(544), 2477–2498. https://doi.org/10.1002/qj.49712354416

Liu, X., Ma, P.-L., Wang, H., Tilmes, S., Singh, B., Easter, R. C., et al. (2016). Description and evaluation of a new four-mode version of the Modal Aerosol Module (MAM4) within version 5.3 of the Community Atmosphere Model. *Geoscientific Model Development*, *9*(2), 505–522. https://doi.org/10.5194/gmd-9-505-2016

19422466, 2023, 9, Downloaded from https://agupubs.onlinelibrary.wiley.com/doi/10.1029/2022MS003579 by Test, Wiley Online Library on [16/10/2023]. See the Terms and Conditions (https://onlinelibrary.wiley.com/terms-and-conditions) on Wiley Online Library for rules of use; OA articles are governed by the applicable Creative Commons License

Livesey, N. J., Read, W. G., Froidevaux, L., Lambert, A., Santee, M. L., Schwartz, M. J., et al. (2021). Investigation and amelioration of long-term instrumental drifts in water vapor and nitrous oxide measurements from the Aura Microwave Limb Sounder (MLS) and their implications for studies of variability and trends. *Atmospheric Chemistry and Physics*, *21*(20), 15409–15430. https://doi.org/10.5194/acp-21-15409-2021

Long, C. S., Fujiwara, M., Davis, S., Mitchell, D. M., & Wright, C. J. (2017). Climatology and interannual variability of dynamic variables in multiple reanalyses evaluated by the SPARC Reanalysis Intercomparison Project (S-RIP). *Atmospheric Chemistry and Physics*, *17*(23), 14593–14629. https://doi.org/10.5194/acp-17-14593-2017

Maliniemi, V., Nesse Tyssøy, H., Smith-Johnsen, C., Arsenovic, P., & Marsh, D. R. (2021). Effects of enhanced downwelling of NO_X on Antarctic upper-stratospheric ozone in the 21st century. *Atmospheric Chemistry and Physics*, *21*(14), 11041–11052. https://doi.org/10.5194/acp-21-11041-2021

Matthes, K., Marsh, D. R., Garcia, R. R., Kinnison, D. E., Sassi, F., & Walters, S. (2010). Role of the QBO in modulating the influence of the 11 year solar cycle on the atmosphere using constant forcings. *Journal of Geophysical Research*, *115*(D18), D18110. https://doi.org/10.1029/2009JD013020

McPeters, R. D., Bhartia, P. K., Haffner, D., Labow, G. J., & Flynn, L. (2013). The version 8.6 SBUV ozone data record: An overview. *Journal of Geophysical Research: Atmospheres*, *118*(14), 8032–8039. https://doi.org/10.1002/jgrd.50597

Meinshausen, M., Vogel, E., Nauels, A., Lorbacher, K., Meinshausen, N., Etheridge, D. M., et al. (2017). Historical greenhouse gas concentrations for climate modelling (CMIP6). *Geoscientific Model Development*, *10*(5), 2057–2116. https://doi.org/10.5194/gmd-10-2057-2017

Meraner, K., & Schmidt, H. (2018). Climate impact of idealized winter polar mesospheric and stratospheric ozone losses as caused by energetic particle precipitation. *Atmospheric Chemistry and Physics*, *18*(2), 1079–1089. https://doi.org/10.5194/acp-18-1079-2018

Mills, M. J., Richter, J. H., Tilmes, S., Kravitz, B., MacMartin, D. G., Glanville, A. A., et al. (2017). Radiative and chemical response to interactive stratospheric sulfate aerosols in fully coupled CESM1(WACCM). *Journal of Geophysical Research: Atmospheres*, *122*(23), 13061–13078. https://doi.org/10.1002/2017JD027006

Mills, M. J., Schmidt, A., Easter, R., Solomon, S., Kinnison, D. E., Ghan, S. J., et al. (2016). Global volcanic aerosol properties derived from emissions, 1990-2014, using CESM1(WACCM). *Journal of Geophysical Research: Atmospheres*, *121*(5), 2332–2348. https://doi.org/10.1002/2015JD024290

Mlawer, E. J., Taubman, S. J., Brown, P. D., Iacono, M. J., & Clough, S. A. (1997). Radiative transfer for inhomogeneous atmospheres: RRTM, a validated correlated-k model for the longwave. *Journal of Geophysical Research*, *102*(D14), 16663–16682. https://doi.org/10.1029/97JD00237

Molod, A., Takacs, L., Suarez, M., & Bacmeister, J. (2015). Development of the GEOS-5 atmospheric general circulation model: Evolution from MERRA to MERRA2. *Geoscientific Model Development*, *8*(5), 1339–1356. https://doi.org/10.5194/gmd-8-1339-2015

Morice, C. P., Kennedy, J. J., Rayner, N. A., & Jones, P. D. (2012). Quantifying uncertainties in global and regional temperature change using an ensemble of observational estimates: The HadCRUT4 data set. *Journal of Geophysical Research*, *117*(D8), D08101. https://doi.org/10.1029/2011JD017187

Mote, P. W., Rosenlof, K. H., McIntyre, M. E., Carr, E. S., Gille, J. C., Holton, J. R., et al. (1996). An atmospheric tape recorder: The imprint of tropical tropopause temperatures on stratospheric water vapor. *Journal of Geophysical Research*, *101*(D2), 3989–4006. https://doi.org/10.1029/95JD03422

National Academies of Sciences, Engineering, and Medicine. (2021). *Reflecting sunlight: Recommendations for solar geoengineering research and research governance*. The National Academies Press. https://doi.org/10.17226/25762

Neely, R. R., III, & Schmidt, A. (2016). VolcanEESM: Global volcanic sulphur dioxide (SO_2) emissions database from 1850 to present.

Neely, R. R., III, Toon, O. B., Solomon, S., Vernier, J.-P., Alvarez, C., English, J. M., et al. (2013). Recent anthropogenic increases in SO_2 from Asia have minimal impact on stratospheric aerosol. *Geophysical Research Letters*, *40*(5), 999–1004. https://doi.org/10.1002/grl.50263

Neu, J. L., Flury, T., Manney, G. L., Santee, M. L., Livesey, N. J., & Worden, J. (2014). Tropospheric ozone variations governed by changes in stratospheric circulation. *Nature Geoscience*, *7*(5), 340–344. https://doi.org/10.1038/ngeo2138

Pedatella, N. M., Richter, J. H., Edwards, J., & Glanville, A. A. (2021). Predictability of the mesosphere and lower thermosphere during major sudden stratospheric warmings. *Geophysical Research Letters*, *48*(15), e2021GL093716. https://doi.org/10.1029/2021GL093716

Pitari, G., Visioni, D., Mancini, E., Cionni, I., Di Genova, G., & Gandolfi, I. (2016). Sulfate aerosols from non-explosive volcanoes: Chemical-radiative effects in the troposphere and lower stratosphere. *Atmosphere*, *7*(7), 85. https://doi.org/10.3390/atmos7070085

Plane, J. M. C. (2012). Cosmic dust in the earth's atmosphere. *Chemical Society Reviews*, *41*(19), 6507–6518. https://doi.org/10.1039/C2CS35132C

Polvani, L. M., Wang, L., Abalos, M., Butchart, N., Chipperfield, M. P., Dameris, M., et al. (2019). Large impacts, past and future, of ozone-depleting substances on Brewer-Dobson circulation trends: A multimodel assessment. *Journal of Geophysical Research: Atmospheres*, *124*(13), 6669–6680. https://doi.org/10.1029/2018JD029516

Price, C., Penner, J., & Prather, M. (1997). NO_x from lightning: 1. Global distribution based on lightning physics. *Journal of Geophysical Research*, *102*(D5), 5929–5941. https://doi.org/10.1029/96JD03504

Quaglia, I., Timmreck, C., Niemeier, U., Visioni, D., Pitari, G., Brodowsky, C., et al. (2023). Interactive stratospheric aerosol models' response to different amounts and altitudes of SO_2 injection during the 1991 Pinatubo eruption. *Atmospheric Chemistry and Physics*, *23*(2), 921–948. https://doi.org/10.5194/acp-23-921-2023

Randel, W. J., Smith, A. K., Wu, F., Zou, C.-Z., & Qian, H. (2016). Stratospheric temperature trends over 1979-2015 derived from combined SSU, MLS, and SABER satellite observations. *Journal of Climate*, *29*(13), 4843–4859. https://doi.org/10.1175/JCLI-D-15-0629.1

Remsberg, E. E., Marshall, B. T., Garcia-Comas, M., Krueger, D., Lingenfelser, G. S., Martin-Torres, J., et al. (2008). Assessment of the quality of the Version 1.07 temperature-versus-pressure profiles of the middle atmosphere from TIMED/SABER. *Journal of Geophysical Research*, *113*(D17), D17101. https://doi.org/10.1029/2008JD010013

Richter, J. H., Sassi, F., & Garcia, R. R. (2010). Toward a physically based gravity wave source parameterization in a general circulation model. *Journal of the Atmospheric Sciences*, *67*(1), 136–156. https://doi.org/10.1175/2009JAS3112.1

Rugenstein, M., Bloch-Johnson, J., Gregory, J., Andrews, T., Mauritsen, T., Li, C., et al. (2020). Equilibrium climate sensitivity estimated by equilibrating climate models. *Geophysical Research Letters*, *47*(4), e2019GL083898. https://doi.org/10.1029/2019GL083898

Scaife, A. A., Athanassiadou, M., Andrews, M., Arribas, A., Baldwin, M., Dunstone, N., et al. (2014). Predictability of the quasi-biennial oscillation and its northern winter teleconnection on seasonal to decadal timescales. *Geophysical Research Letters*, *41*(5), 1752–1758. https://doi.org/10.1002/2013GL059160

Schweiger, A., Lindsay, R., Zhang, J., Steele, M., Stern, H., & Kwok, R. (2011). Uncertainty in modeled Arctic sea ice volume [Dataset]. Journal of Geophysical Research, *116*(C8), C00D06. https://doi.org/10.1029/2011JC007084

Scinocca, J. F., & McFarlane, N. A. (2000). The parametrization of drag induced by stratified flow over anisotropic orography. *Quarterly Journal of the Royal Meteorological Society*, *126*(568), 2353–2393. https://doi.org/10.1002/qj.49712656802

19422466, 2023, 9, Downloaded from https://agupubs.onlinelibrary.wiley.com/doi/10.1029/2022MS003579 by Test, Wiley Online Library on [16/10/2023]. See the Terms and Conditions (https://onlinelibrary.wiley.com/terms-and-conditions) on Wiley Online Library for rules of use; OA articles are governed by the applicable Creative Commons License

Sherwood, S. C., Webb, M. J., Annan, J. D., Armour, K. C., Forster, P. M., Hargreaves, J. C., et al. (2020). An assessment of earth's climate sensitivity using multiple lines of evidence. *Reviews of Geophysics*, *58*(4), e2019RG000678. https://doi.org/10.1029/2019RG000678

Sinnhuber, M., Berger, U., Funke, B., Nieder, H., Reddmann, T., Stiller, G., et al. (2018). NO_y production, ozone loss and changes in net radiative heating due to energetic particle precipitation in 2002-2010. *Atmospheric Chemistry and Physics*, *18*(2), 1115–1147. https://doi.org/10.5194/acp-18-1115-2018

Sinnhuber, M., Nieder, H., & Wieters, N. (2012). Energetic particle precipitation and the chemistry of the mesosphere/lower thermosphere. *Surveys in Geophysics*, *33*(6), 1281–1334. https://doi.org/10.1007/s10712-012-9201-3

Smith, A. K., Garcia, R. R., Marsh, D. R., & Richter, J. H. (2011). WACCM simulations of the mean circulation and trace species transport in the winter mesosphere. *Journal of Geophysical Research*, *116*(D20), D20115. https://doi.org/10.1029/2011JD016083

Solomon, S. (1999). Stratospheric ozone depletion: A review of concepts and history. *Reviews of Geophysics*, *37*(3), 275–316. https://doi.org/10.1029/1999RG900008

Solomon, S., Dube, K., Stone, K., Yu, P., Kinnison, D., Toon, O. B., et al. (2022). On the stratospheric chemistry of midlatitude wildfire smoke. *Proceedings of the National Academy of Sciences*, *119*(10), e2117325119. https://doi.org/10.1073/pnas.2117325119

Solomon, S., Garcia, R., Rowland, F. S., & Wuebbles, D. J. (1986). On the depletion of Antarctic ozone. *Nature*, *321*(6072), 755–758. https://doi.org/10.1038/321755a0

Thomason, L. W., Ernest, N., Millán, L., Rieger, L., Bourassa, A., Vernier, J.-P., et al. (2018). A global space-based stratospheric aerosol climatology: 1979–2016. *Earth System Science Data*, *10*(1), 469–492. https://doi.org/10.5194/essd-10-469-2018

Tilmes, S., Hodzic, A., Emmons, L. K., Mills, M. J., Gettelman, A., Kinnison, D. E., et al. (2019). Climate forcing and trends of organic aerosols in the Community Earth System Model (CESM2). *Journal of Advances in Modeling Earth Systems*, *11*(12), 4323–4351. https://doi.org/10.1029/2019MS001827

Tilmes, S., MacMartin, D. G., Lenaerts, J. T. M., van Kampenhout, L., Muntjewerf, L., Xia, L., et al. (2020). Reaching 1.5 and 2.0° global surface temperature targets using stratospheric aerosol geoengineering. *Earth System Dynamics*, *11*(3), 579–601. https://doi.org/10.5194/esd-11-579-2020

Tilmes, S., Richter, J. H., Kravitz, B., MacMartin, D. G., Glanville, A. S., Visioni, D., et al. (2021). Sensitivity of total column ozone to stratospheric sulfur injection strategies. *Geophysical Research Letters*, *48*(19), e2021GL094058. https://doi.org/10.1029/2021GL094058

Tilmes, S., Visioni, D., Jones, A., Haywood, J., Séférian, R., Nabat, P., et al. (2022). Stratospheric ozone response to sulfate aerosol and solar dimming climate interventions based on the G6 Geoengineering Model Intercomparison Project (GeoMIP) simulations. *Atmospheric Chemistry and Physics*, *22*(7), 4557–4579. https://doi.org/10.5194/acp-22-4557-2022

Toms, B. A., Barnes, E. A., Maloney, E. D., & van den Heever, S. C. (2020). The global teleconnection signature of the Madden-Julian oscillation and its modulation by the quasi-biennial oscillation. *Journal of Geophysical Research: Atmospheres*, *125*(7), e2020JD032653. https://doi.org/10.1029/2020JD032653

van Marle, M. J. E., Kloster, S., Magi, B. I., Marlon, J. R., Daniau, A.-L., Field, R. D., et al. (2016). *Biomass burning emissions for CMIP6 (v1.2)*. Earth System Grid Federation. https://doi.org/10.22033/ESGF/input4MIPs.1117

van Marle, M. J. E., Kloster, S., Magi, B. I., Marlon, J. R., Daniau, A.-L., Field, R. D., et al. (2017). Historic global biomass burning emissions for CMIP6 (BB4CMIP) based on merging satellite observations with proxies and fire models (1750–2015). *Geoscientific Model Development*, *10*(9), 3329–3357. https://doi.org/10.5194/gmd-10-3329-2017

Verronen, P. T., Andersson, M. E., Marsh, D. R., Kovács, T., & Plane, J. M. C. (2016). WACCM-D: Whole Atmosphere Community Climate Model with D-region ion chemistry. *Journal of Advances in Modeling Earth Systems*, *8*(2), 954–975. https://doi.org/10.1002/2015MS000592

Visioni, D., MacMartin, D. G., Kravitz, B., Boucher, O., Jones, A., Lurton, T., et al. (2021). Identifying the sources of uncertainty in climate model simulations of solar radiation modification with the G6sulfur and G6solar Geoengineering Model Intercomparison Project (GeoMIP) simulations. *Atmospheric Chemistry and Physics*, *21*(13), 10039–10063. https://doi.org/10.5194/acp-21-10039-2021

Visioni, D., MacMartin, D. G., Kravitz, B., Lee, W., Simpson, I. R., & Richter, J. H. (2020). Reduced poleward transport due to stratospheric heating under stratospheric aerosols geoengineering. *Geophysical Research Letters*, *47*(17), e2020GL089470. https://doi.org/10.1029/2020GL089470

Visioni, D., Tilmes, S., Bardeen, C., Mills, M., MacMartin, D. G., Kravitz, B., & Richter, J. H. (2022). Limitations of assuming internal mixing between different aerosol species: A case study with sulfate geoengineering simulations. *Atmospheric Chemistry and Physics*, *22*(3), 1739–1756. https://doi.org/10.5194/acp-22-1739-2022

Waugh, D., & Hall, T. (2002). Age of stratospheric air: Theory, observations, and models. *Reviews of Geophysics*, *40*(4), 1-1–1-26. https://doi.org/10.1029/2000RG000101

Weisenstein, D. K., Visioni, D., Franke, H., Niemeier, U., Vattioni, S., Chiodo, G., et al. (2022). An interactive stratospheric aerosol model intercomparison of solar geoengineering by stratospheric injection of SO_2 or accumulation-mode sulfuric acid aerosols. *Atmospheric Chemistry and Physics*, *22*(5), 2955–2973. https://doi.org/10.5194/acp-22-2955-2022

Zelinka, M. D., Myers, T. A., McCoy, D. T., Po-Chedley, S., Caldwell, P. M., Ceppi, P., et al. (2020). Causes of higher climate sensitivity in CMIP6 models. *Geophysical Research Letters*, *47*(1), e2019GL085782. https://doi.org/10.1029/2019GL085782

Zhang, G. J., & McFarlane, N. M. (1995). Sensitivity of climate simulations to the parameterization of cumulus convection in the Canadian Climate Centre general circulation model. *Atmosphere-Ocean*, *33*(3), 407–446. https://doi.org/10.1080/07055900.1995.9649539

Zhang, J., & Rothrock, D. A. (2003). Modeling global sea ice with a thickness and enthalpy distribution model in generalized curvilinear coordinates. *Monthly Weather Review*, *131*(5), 845–861. https://doi.org/10.1175/1520-0493(2003)131⟨0845:MGSIWA⟩2.0.CO;2

Zhang, J., Wuebbles, D., Kinnison, D., & Baughcum, S. L. (2021). Stratospheric ozone and climate forcing sensitivity to cruise altitudes for fleets of potential supersonic transport aircraft. *Journal of Geophysical Research: Atmospheres*, *126*(16), e2021JD034971. https://doi.org/10.1029/2021JD034971

Zhu, J., Otto-Bliesner, B. L., Brady, E. C., Gettelman, A., Bacmeister, J. T., Neale, R. B., et al. (2022). LGM paleoclimate constraints inform cloud parameterizations and equilibrium climate sensitivity in CESM2. *Journal of Advances in Modeling Earth Systems*, *14*(4), e2021MS002776. https://doi.org/10.1029/2021MS002776

Ziemke, J. R., Chandra, S., Duncan, B. N., Froidevaux, L., Bhartia, P. K., Levelt, P. F., & Waters, J. W. (2006). Tropospheric ozone determined from Aura OMI and MLS: Evaluation of measurements and comparison with the Global Modeling Initiative's Chemical Transport Model. *Journal of Geophysical Research*, *111*(D19), D19303. https://doi.org/10.1029/2006JD007089

Ziemke, J. R., Oman, L. D., Strode, S. A., Douglass, A. R., Olsen, M. A., McPeters, R. D., et al. (2019). Trends in global tropospheric ozone inferred from a composite record of TOMS/OMI/MLS/OMPS satellite measurements and the MERRA-2 GMI simulation. *Atmospheric Chemistry and Physics*, *19*(5), 3257–3269. https://doi.org/10.5194/acp-19-3257-2019

19422466, 2023, 9, Downloaded from https://agupubs.onlinelibrary.wiley.com/doi/10.1029/2022MS003579 by Test, Wiley Online Library on [16/10/2023]. See the Terms and Conditions (https://onlinelibrary.wiley.com/terms-and-conditions) on Wiley Online Library for rules of use; OA articles are governed by the applicable Creative Commons License